

Chapter 6

Neutron induced (n, p) reaction cross section for ^{76}Se , ^{77}Se , ^{78}Se , ^{80}Se , ^{65}Cu , ^{52}Cr , ^{51}V and ^{48}Ti isotopes

6.1. Introduction

The cross sections measurements of neutron induced (n, p) reaction on structural materials is essential for the construction of the International Thermonuclear Experimental Reactor (ITER) and Accelerator Driven Sub-Critical System (ADSs), fourth-generation nuclear reactors above 15 MeV neutron energies, fission power plants, accelerators, astrophysics, space dosimetry, shielding applications as well as production of the medical isotopes for radiation therapy. Besides this, the neutron induced charged particle emission (n, p) and (n, α) reactions cross sections data are also helpful in the nuclear heating, induced radioactivity, nuclear transmutation rates, and radiation damage of the structural materials due to gas formation on the first wall of the materials. Neutrons and α -particles are produced by the D-T reaction and 80% of the energy carried by neutrons (≈ 14 MeV neutrons) is transferred to the first wall and breeding blanket of the fusion reactor. The remaining energies are carried by α -particles, charged particles and low energy neutrons, which induce sputtering, erosion and blistering in the plasma-facing materials [1, 2].

Besides, the study of the neutron induced reactions on different nuclei provides an experimental archive to assess the relevance of the theoretical models of nuclear physics for practical applications. The experimental results help to evaluate the statistical model code and limit the parameter set used therein. Such studies can also provide valuable insight into the reaction mechanisms that dominate different regions of energy. It should be noted that updating the evaluated cross sections depends on the availability of accurate measurements obtainable from advanced neutron sources [3].

The use of copper as a first wall material has been considered in reactor designs that have high thermal loads on the first wall or require a shield of high electrically conductive material surrounding the plasma to help stabilize its location. Other designs

also use copper as a heat sink with other materials for highly loaded diverter collector plates. Copper alloys are also considered for the electrically conducting central column of the close aspect ratio tokamaks for the new concept of compact fusion machines [4-5]. Similarly, Vanadium based alloys have excellent properties that make them an essential structural material for reactor technology. In the fusion reactor, vanadium is considered the reactor structural material for the first wall/blanket applications due to the low activation properties of the vanadium alloys. The vanadium based alloys have high thermal conductivity and lower thermal expansion coefficient, which lowers thermal stress for a given temperature than other alloys and enhances reactor lifetime capability and wall load. The lower helium generation rate, lower bulk nuclear heating rate and better tritium breeding performance due to lower neutron absorption are shown by the vanadium based alloys. Thus, it is essential to study the higher energy neutron induced reaction cross section of vanadium from an application point of view [6].

Titanium alloys are desirable structural materials for fusion reactors because of their great characteristics. Titanium has a high strength-to-weight ratio, intermediate strength values, good fatigue and creep rupture properties, small modulus of elasticity, high electrical resistivity, heat capacity, low coefficient of thermal expansion, low long-term residual radioactivity, high corrosion resistance, good compatibility with coolants such as lithium, helium, and water, high workability and weldability, and commercial availability with established mine and mill facilities. Since chromium is an important constituent of structural steel, its activation data is important for practical applications in fusion reactor technology ~e.g., estimation of activity level, hydrogen and helium gas production, nuclear heating, and radiation damage [7-8].

The ^{78}Se and ^{80}Se isotopes are also used as targets to produce ^{77}Br and $^{80\text{m}}\text{Br}$, which are therapeutic radioisotopes. The (n, p) reaction produces arsenic isotopes, which are very much poisonous to humans and other living creatures. Cancer and other serious health problems occur due to the arsenic element. Therefore, the measurement of the $\text{Se}(n, p)\text{As}$ reaction cross section is important to produce arsenic from the selenium. Due to discrepancies in data, it is very complex to fix and improve the statistical model parameters. Therefore, new experimentally measured data with better accuracy are needed for understanding different reaction channels by comparing this with the suitable statistical model [9].

The systematic study of gas producing reaction (n, p) is needed for structural materials because this reaction is harmful to the mechanical stability of the reactor. Several authors

studied the (n,p) reaction cross section of the ^{65}Cu , ^{52}Cr , ^{51}V and ^{48}Ti isotopes. These experimental cross sections data reported in the EXFOR database [10] were measured using neutrons from the D-D and D-T reactions, whereas only one datum in the quasi-monoenergetic neutrons was produced based on $^9\text{Be}(p,n)$ reaction neutrons. The (n,p) reaction cross section has been thoroughly investigated within 13-15 MeV neutron energies and these available experimental data agree very well with each other below 13 MeV but reveal huge discrepancies in cross section above 15 MeV. There are also significant differences in the evaluated (n,p) reaction cross section above the neutron energy of 14 MeV, which were found in many Evaluated Nuclear Data File (ENDF) libraries [11-20]. Due to the significant spread in the measured cross section values, it is not surprising that the evaluated (n,p) reaction cross section varies significantly above the neutron energies of 15 MeV, making it very uncertain extrapolating to higher energies. The significant discrepancies in the measured (n,p) reaction cross section above 15 MeV were the main reason for the present study at higher energies.

The cross sections of the $^{76}\text{Se}(n,p)^{76}\text{As}$, $^{77}\text{Se}(n,p)^{77}\text{As}$, $^{78}\text{Se}(n,p)^{78}\text{As}$, $^{80}\text{Se}(n,p)^{80}\text{As}$, $^{51}\text{V}(n,p)^{51}\text{Ti}$ and $^{65}\text{Cu}(n,p)^{65}\text{Ni}$ reactions were measured above 7 MeV neutron energies relative to the $^{27}\text{Al}(n,\alpha)^{24}\text{Na}$ reference reaction using the activation and offline γ -ray spectrometric technique. The present results were compared with the experimental data taken from the EXFOR database and evaluations of the ENDF/B-VIII.0, JEFF-3.3, JENDL-4.0/HE, CENDL-3.2, TENDL-2019 and FENDL-3.2 libraries. The statistical nuclear reaction TALYS (ver. 1.9) [21] and EMPIRE (ver. 3.2.3) [22] codes were used to calculate the cross sections using different optical potential, level density and pre-equilibrium model options as given in the codes with the default and modified input parameters. In theoretical calculations from statistical codes, suitable model selection is essential to reproduce the measured and reported reaction cross section values. Furthermore, the systematic theoretical study of cross sections for fusion reactor structure materials Ti and Cr was performed by the TALYS code. The statistical model calculations were discussed and compared with the available experimental and evaluated data. The uncertainties in the present measured cross sections were calculated through partial uncertainties in different attributes and correlations among these data by the method of covariance analysis techniques. This covariance matrix gives complete information about the error in the present measured (n,p) reaction cross sections. In addition, the calculation from

systematic formulae was performed within 14-15 MeV neutron energies for estimation of (n, p) reaction cross sections of Se, V, Cu, Cr and Ti isotopes, and these calculated values of cross sections were compared with the previous experimental data. It will help to improve cross sections within 14-15 MeV energies.

6.2. Theoretical calculations using the EMPIRE and TALYS codes for the ^{76}Se , ^{77}Se , ^{78}Se , ^{80}Se , ^{65}Cu , ^{52}Cr , ^{51}V and ^{48}Ti

The theoretical estimation of cross sections for the $^{76}\text{Se}(n, p)^{76}\text{As}$, $^{77}\text{Se}(n, p)^{77}\text{As}$, $^{78}\text{Se}(n, p)^{78}\text{As}$, $^{80}\text{Se}(n, p)^{80}\text{As}$, $^{48}\text{Ti}(n, p)^{48}\text{Sc}$, $^{51}\text{V}(n, p)^{51}\text{Ti}$, $^{52}\text{Cr}(n, p)^{52}\text{V}$ and $^{65}\text{Cu}(n, p)^{65}\text{Ni}$ reactions were performed by using two different statistical nuclear model computer codes TALYS (ver. 1.9) and EMPIRE (ver. 3.2.3) within the neutron energies of reaction threshold to 25 MeV. These two are the statistical reaction codes including direct reaction (DI), pre-equilibrium emission (PE) and compound nucleus (CN) reaction mechanisms. The present results as well as the previous ones were compared with the theoretically calculated values based on the TALYS and EMPIRE codes.

6.2.1 Calculation of (n, p) reaction cross section using TALYS code

The calculation of cross sections using the TALYS code contributes to the compound nucleus by the Hauser-Feshbach theory [23]. The preequilibrium contribution models based on the exciton model [24] and multistep compound (MSC) and multistep direct (MSD) [25] were used in the calculations. In the direct reaction calculation, the default option used is the coupled channels model. In addition, the optical potential mentioned by Koning-Delaroche [26] and Bauge-Delaroche [27] was used to obtain optical model parameters for neutrons and protons from the RIPL-3 [28] database. To consider the γ -ray emission channel competition in reaction, TALYS uses a fixed γ -ray strength function model. The Brink-Axel Lorentzian [29-30] was implemented for the γ -ray strength functions for all the transitions and the Kopecky-Uhl generalized Lorentzian [31] is used for the E1 transitions.

The six different phenomenological and microscopic nuclear level density models are used for the estimation of nuclear reaction cross section. These models range from

phenomenological analytical expressions to tabulated level densities derived from microscopic models. The phenomenological level density models are as follows:

- I. In the constant temperature model introduced by Gilbert-Cameron [32], the excitation energy is divided into two-parts: the lower energy part where the constant temperature law applies and the higher energy part where the Fermi gas model applies.
- II. In the back-shifted Fermi gas model [33], the Fermi gas expression is used in all the excitation energy regions.
- III. In the generalized superfluid model [34–35], superconductive pairing correlations are considered according to the Barden-Cooper-Schrieffer theory, *i.e.*, low energy pairing correlations strongly influence the level density. In contrast, the high energy region is described by the Fermi gas model.

The other three microscopic level density models are as follows:

- I. In ldmodel 4 for the RIPL database, Goriely has calculated level densities from drip line to drip line based on Hartree-Fock calculations for excitation energies up to 150 MeV and spin values up to $I = 30$ [36].
- II. In ldmodel 5 the calculations make coherent use of nuclear structure properties determined within the deformed Skyrme-Hartree-Fock-Bogoliubov framework [37].
- III. The ldmodel 6 is based on temperature-dependent Hartree-Fock-Bogoliubov calculations using the Gogny force [38].

The D_0 is the s-wave average neutron resonance spacing in keV at the neutron separation energy and it is related to the level density according to the following formula:

$$\frac{1}{D_0} = \sum_{J=|I-\frac{1}{2}|}^{J=|I+\frac{1}{2}|} \rho(S_n, J, \Pi) \quad (1)$$

The experimental value of D_0 for the ^{65}Cu was obtained from the RIPL-3 database and compared with the theoretical values predicted for each level density model by TALYS code. The values of the D_0 are mentioned in Table 6.1.

Table 6.1 The experimental value of D_0 for the ^{65}Cu was obtained from the RIPL-3 database and compared with the theoretical values predicted for each level density model by TALYS (ver. 1.9) code.

Level density model	Experimental value of D_0 (keV)	Theoretical value of D_0 (keV)
Constant temperature	1.3 ± 0.11	0.3179
Back-shifted Fermi gas		0.6025
Generalized superfluid		0.5758
S. Goriely (microscopic 1)		0.7782
S. Goriely-S. Hilaire (microscopic 2)		0.4051
S. Goriely-S. Hilaire Gogny force		0.6720
(microscopic 3)		

The parameter α is the energy dependent level density parameter, which considers the existence of shell effects at low energies and the damping of the latter as the excitation energy increases according to the following equation:

$$\alpha = \alpha(E_x) = \hat{\alpha} \left(1 + \delta W \left(\frac{1 - \exp(-\gamma U)}{U} \right) \right) \quad (2)$$

The terms δW and γ stand for the shell correction energy and the γ damping parameter of shell effects with increasing excitation energy, and $U = (E_x - \Delta)$ where this energy shift Δ adjustable empirical parameter is closely related to the pairing energy and includes odd-even effects in nuclei respectively. The parameter $\hat{\alpha}$ is called the asymptotic level density parameter and is equal to α when shell effects are absent. The asymptotic value $\tilde{\alpha}$ is given by the smooth form:

$$\tilde{\alpha} = \alpha A + \beta A^{2/3} \quad (3)$$

Where A is the mass number, α and β are the variable parameters, and the value of $\tilde{\alpha}$ obtains in the absence of any shell effects. The damping parameter γ is given by the following formula systematically

$$\gamma = \frac{\gamma_1}{A^{1/3}} + \gamma_2 \quad (4)$$

Similarly, two other parameters ‘‘ptable’’ and ‘‘pair’’ for the microscopic level density models were adjusted to fit the present measurements and literature data. A brief discussion of microscopic level density and its parameters is given in the TALYS manual. These

adjustments in theoretical calculations are helpful to identify the parameters that have a significant effect on cross section values.

The level density models with default input parameters were not viable for producing cross sections that agree well with the experimental data taken from the EXFOR database. Therefore, various input parameters are adjusted in the TALYS code to reproduce the admissible cross sections for the entire neutron energy range. It is assumed that nuclear reactions are dependent on the nuclear level densities (NLDs), optical model potentials (OMPs) and γ -ray strength functions (γ -SFs). The description of the different theoretical models of the TALYS code is given in Table 6.2. The preequilibrium contribution, which becomes essential for incident energies above almost 10 MeV is modelled using the two-component exciton model. The combinations for input parameters were considered to determine the theoretical variation in cross sections and the sensitivity of the cross sections to each nuclear model.

6.2.2 Calculation of (n, p) reaction cross section using EMPIRE code

In addition, the theoretical calculations were performed using the EMPIRE (ver. 3.2.3) [22] code. In the EMPIRE code, the CN reaction cross section was calculated in the framework of the Hauser-Feshbach theory [23]. The calculation of the direct reaction was considered using the ECIS06 code [39]. The width fluctuation corrections were considered using the Hofmann, Richert, Tepel, and Weidenmuller model [40-42] up to an incident neutron energy of 3 MeV. The optical potential model parameters for the outgoing protons were also taken from the RIPL-3 [28] database using Koning and Delaroche [26]. The γ -ray strength function was described via the modified Lorentzian model [43] available in the RIPL-3 database. The different level density models, namely, (i) Gilbert-Cameron [32], (ii) generalized superfluid [34-35], and (iii) Hartree-Fock-BCS approach [36], were used for estimating the cross sections from threshold to 25 MeV. Moreover, the quantum-mechanical preequilibrium models (i) MSC [44] and (ii) MSD [45] and the phenomenological preequilibrium models (i) exciton model with default mean free path multiplier (PCROSS = 1.5) [46] and (ii) Monte Carlo hybrid (DDHMS) [47] were implemented to consider the preequilibrium emission at higher energies in the (n, p) reaction cross section of the ^{76}Se ,

^{77}Se , ^{78}Se , ^{80}Se , ^{65}Cu , ^{52}Cr , ^{51}V and ^{48}Ti nuclei. The description of the different theoretical models of the EMPIRE code is given in Table 6.2.

Table 6.2 The statistical model codes used for the default theoretical calculations of the (n, p) reaction cross section of the ^{76}Se , ^{77}Se , ^{78}Se , ^{80}Se , ^{65}Cu , ^{52}Cr , ^{51}V and ^{48}Ti nuclei.

Statistical codes	Optical potential model	Level density models	Pre-equilibrium model	γ -ray strength function model
EMPIRE (ver. 3.2.3)	Koning-Delaroche	Generalized superfluid Gilbert-Cameron Hartree-Fock-BCS (HF-BCS)	Multi-Step-Compound (MSC) Multi-Step-Direct (MSD) Exciton model (PCROSS) Monte Carlo Hybrid (DDHMS)	Modified Lorentzian (MLO1)
TALYS (ver. 1.95)	Koning-Delaroche local Koning-Delaroche global Koning-Delaroche dispersive Bauge-Delaroche	Constant temperature Back-shifted Fermi gas Generalized superfluid S. Goriely S. Goriely-S. Hilaire S. Goriely-S. Hilaire Gogny force	preeqmode 1 preeqmode 2 preeqmode 3 preeqmode 4	Kopecky-Uhl strength 1: Kopecky-Uhl generalized Lorentzian

6.3. Results and Discussion of Se, Cu, V, Ti and Cr Elements

It is observed that most of the previous measurements were made with β -ray or γ -ray counting using NaI(Tl) detector. The γ -ray counting with NaI(Tl) detector suffers from a defect of poor resolution. There are very few measurements reported with Ge(Li) detector. Therefore, the discrepancies were observed in reported (n, p) reaction cross sections. In addition, to explore the discrepancies among the measured (n, p) reaction cross sections of the ^{65}Cu , ^{52}Cr , ^{51}V and ^{48}Ti fusion reactor structure materials and ^{76}Se , ^{77}Se , ^{78}Se , ^{80}Se nuclei the theoretical estimations were conducted using the statistical TALYS and EMPIRE codes.

6.3.1 Selenium (Se)

The cross sections of the $^{76}\text{Se}(n,p)^{76}\text{As}$, $^{77}\text{Se}(n,p)^{77}\text{As}$, $^{78}\text{Se}(n,p)^{78}\text{As}$ and $^{80}\text{Se}(n,p)^{80}\text{As}$ reactions were measured relative to the $^{27}\text{Al}(n,\alpha)^{24}\text{Na}$ monitor reaction at 10.50 ± 0.68 , 13.52 ± 0.67 , 16.86 ± 0.55 and 19.81 ± 0.59 MeV neutron energies.

6.3.1.1 The $^{76}\text{Se}(n,p)^{76}\text{As}$ excitation function

The measured cross section for the $^{76}\text{Se}(n,p)^{76}\text{As}$ reaction with their uncertainties are presented in Table 3.8 [Chapter 3]. The theoretical estimates of $^{76}\text{Se}(n,p)^{76}\text{As}$ reaction cross section have been performed within 4 to 22 MeV by EMPIRE code with different level density and nucleon potential as well as by TALYS code with *ldmodel* 1 to 6 and nucleon potential by considering exciton model *preeqmode* 2. The measured cross section of $^{76}\text{Se}(n,p)^{76}\text{As}$ reaction discussed and compared with the data from EMPIRE and TALYS codes, evaluated data of JENDL-4.0, TENDL-2019 and ENDF/B-VIII.0 libraries as well as with the literature data taken from EXFOR compilation as shown in Fig. 6.1. The large difference between ENDF/B-VIII.0 and JENDL-4.0, TENDL-2019 evaluated data can be seen in 7 to 14 MeV energy range and at higher energy. The experimental data obtained in the present work at 10.50 MeV agree well with the existing literature data of I. Birn *et al.* [48], with theoretical calculation obtained from TALYS code using *ldmodel* 2 as shown in Fig. 6.1(b) and with EMPIRE code using LEVDEN 4 as shown in Fig. 6.1(a). It is observed that at 13.52 MeV, the TENDL-2019 and JENDL-4.0 predictions and above 16 MeV energies the TENDL-2019 and ENDF/B-VIII.0 evaluated data agree with the present data. The JENDL-4.0 evaluation overestimates data above 14 MeV. The cross sections were measured for the first time at 16.86 and 19.81 MeV energies. At higher energies the measured cross sections agree well with the theoretically calculated values obtained from the EMPIRE code with LEVDEN 3 model as shown in Fig. 6.1(a) and with TALYS calculation with level density models *ldmodel* 4 and 5 as shown in Fig. 6.1(b).

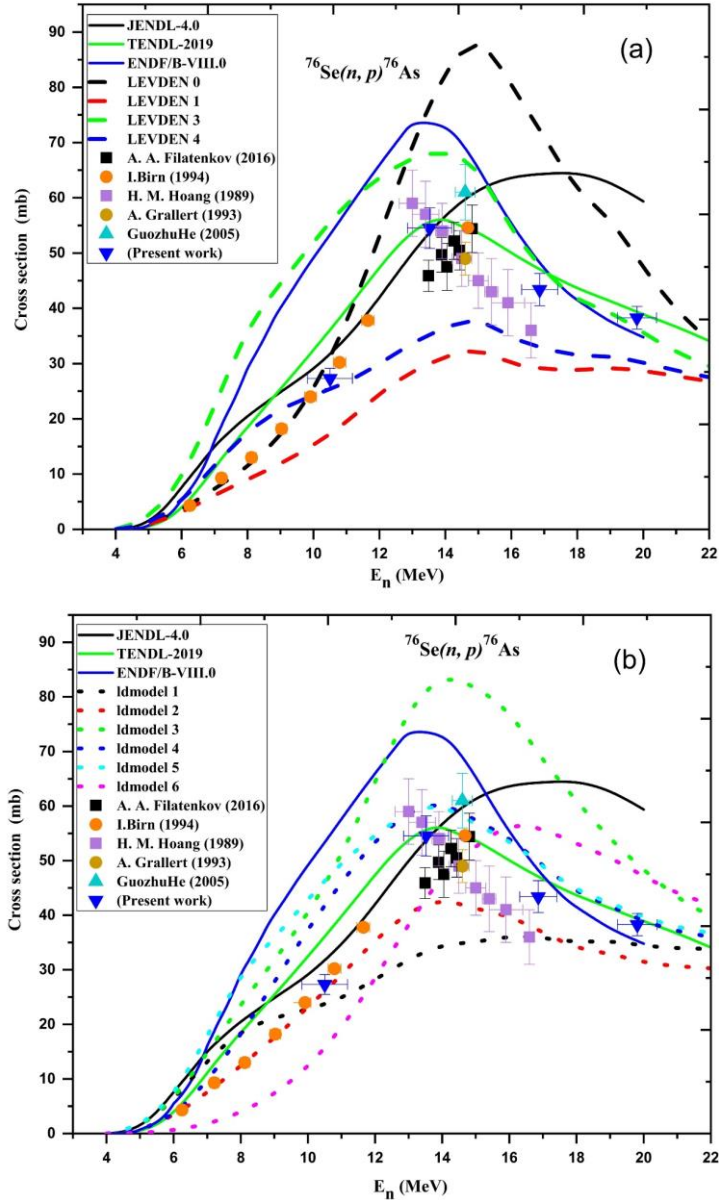
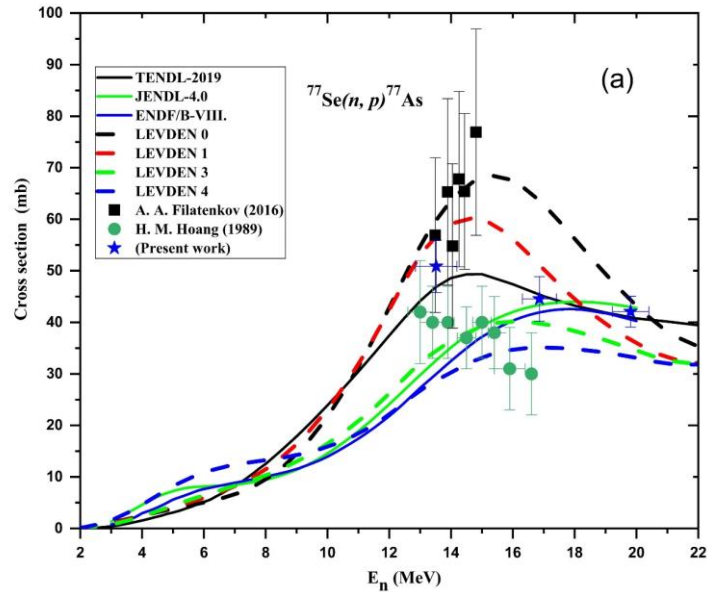


Fig. 6.1. (a) and (b) Comparison of the $^{76}\text{Se}(n, p)^{76}\text{As}$ reaction cross sections with literature data from EXFOR compilation, with JENDL, TENDL and ENDF evaluated libraries and with the theoretical results obtained from EMPIRE and TALYS codes.

6.3.1.2 The $^{77}\text{Se}(n, p)^{77}\text{As}$ excitation function

The measured cross section for the $^{77}\text{Se}(n, p)^{77}\text{As}$ reaction with their uncertainties are presented in Table 3.8 [Chapter 3]. The theoretical estimates of $^{77}\text{Se}(n, p)^{77}\text{As}$ reaction cross section have been performed in the neutron energies region of 2 to 22 MeV by EMPIRE code with different level density and nucleon potential as well as by TALYS code with ldmodel 1 to 6 and nucleon potential by considering exciton model preeqmode 2. The measured cross

section of $^{77}\text{Se}(n,p)^{77}\text{As}$ reaction discussed and compared with evaluated data of JENDL-4.0, TENDL-2019 and ENDF/B-VIII.0 libraries, literature data taken from EXFOR compilation, as well as with theoretical values obtained from EMPIRE and TALYS codes as shown in Fig. 6.2. The TENDL-2019 evaluation is higher in the 7 to 18 MeV energy region compared to the JENDL-4.0 and ENDF/B-VIII.0. It observed that at 13.52 MeV, the present data is in between the data of H. M. Hoang *et al.* [49] and A. A. Filatenkov [50] within the experimental uncertainties but excellent agreement was found with the theoretical value of TALYS nuclear model calculation of ldmmodel 5 as shown in Fig. 6.2(b). At higher energies 16.86 and 19.81 MeV, the data were measured for the first time. Our data at higher energies agree very well with the evaluated data of JENDL-4.0, TENDL-2019 and ENDF/B-VIII.0 libraries. The measured cross section at 19.81 MeV agrees very well with the theoretical calculation obtained from the EMPIRE code using LEVDEN 0 as shown in Fig. 6.2(a). It can also be seen that the data presented in this work exceeds the values found by H. M. Hoang *et al.* [49].



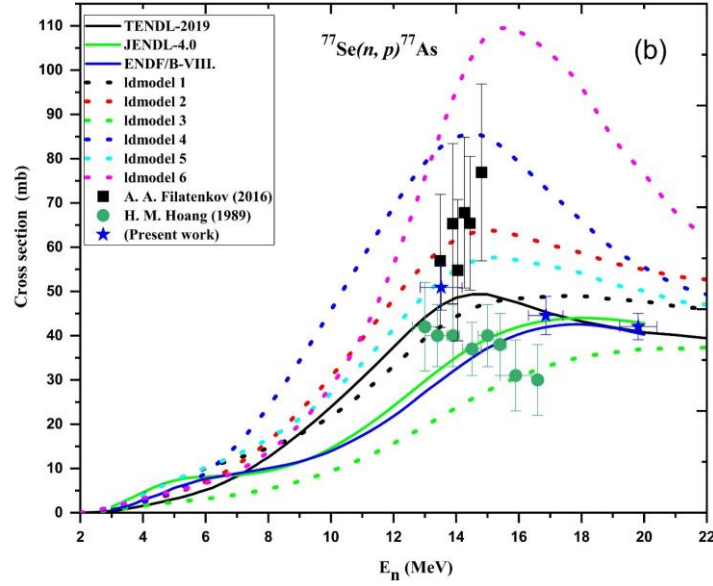


Fig. 6.2. (a) and (b) Comparison of the $^{77}\text{Se}(n,p)^{77}\text{As}$ reaction cross section with literature data from EXFOR compilation, with JENDL, TENDL and ENDF evaluated libraries and with the theoretical results obtained from EMPIRE and TALYS codes.

6.3.1.3 The $^{78}\text{Se}(n,p)^{78}\text{As}$ excitation function

The measured cross section for the $^{78}\text{Se}(n,p)^{78}\text{As}$ reaction with their uncertainties are presented in Table 3.8 [Chapter 3]. The theoretical estimate of $^{78}\text{Se}(n,p)^{78}\text{As}$ reaction cross sections have been performed by EMPIRE code with different level density and nucleon potential as well as by TALYS code with ldmodel 1 to 6 and nucleon potential by considering exciton model preeqmode 2. The measured cross section for the $^{78}\text{Se}(n,p)^{78}\text{As}$ reaction discussed and compared with the theoretical values obtained from the EMPIRE and TALYS codes, evaluated data of JENDL-4.0, TENDL-2019 and ENDF/B-VIII.0 libraries as well as with the literature data taken from EXFOR compilation as shown in Fig. 6.3. The TENDL-2019 evaluation is very high in between 12 to 22 MeV region compared to the JENDL-4.0 and ENDF/B-VIII.0. The present result at 10.50 MeV shows agreement with the theoretical results obtained from the TALYS nuclear model calculation with ldmodel 2, 5 and 6 as shown in Fig. 6.3(b). It is observed that our result at 13.52 MeV agree very well with the existing cross section reported by A. A. Filatenkov [50], Guozhuhe *et al.* [51] within the experimental uncertainties. The theoretical calculation obtained from the EMPIRE nuclear model calculation with LEVDEN 1 and with evaluated of JENDL-4.0 library shows agreement at 13.52 MeV as shown in Fig. 6.3(a). The present experimental result at 16.86 MeV agrees well with the existing data of H. M. Hoang *et al.* [49] within the experimental

uncertainties. Our data at higher energies 19.81 MeV is the first experimental measured data and shows excellent agreement with the theoretical values obtained from EMPIRE code using LEVDEN 3 as shown in Fig. 6.3(a).

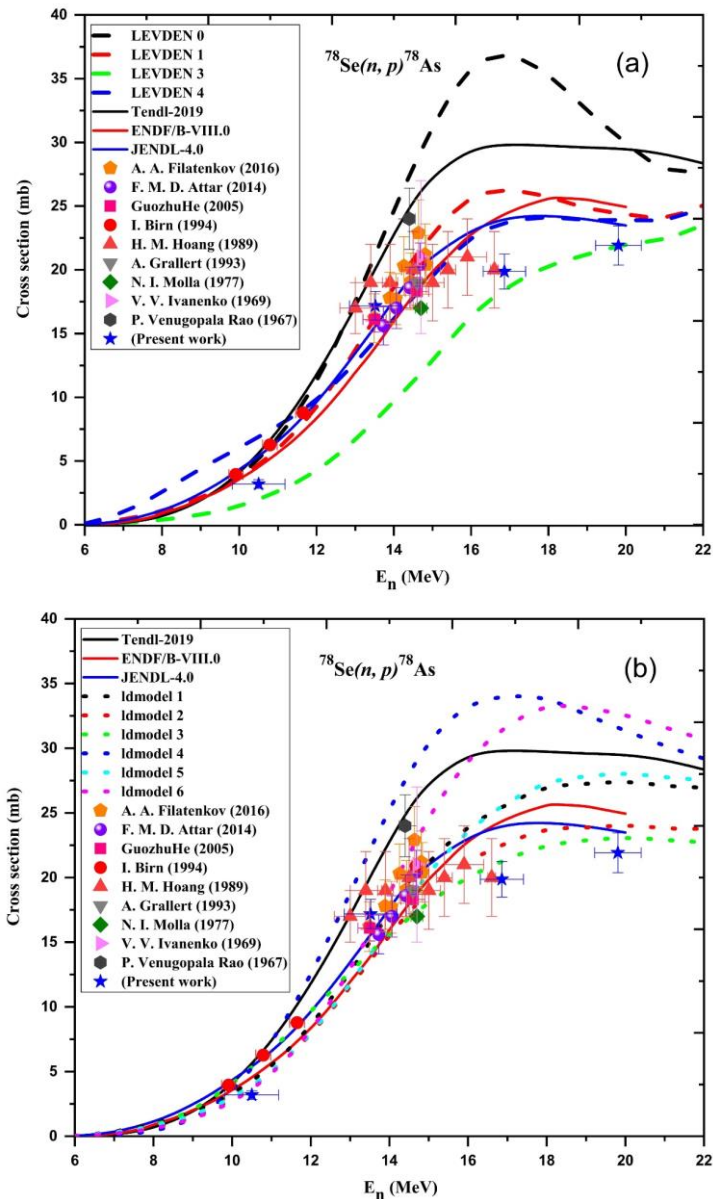
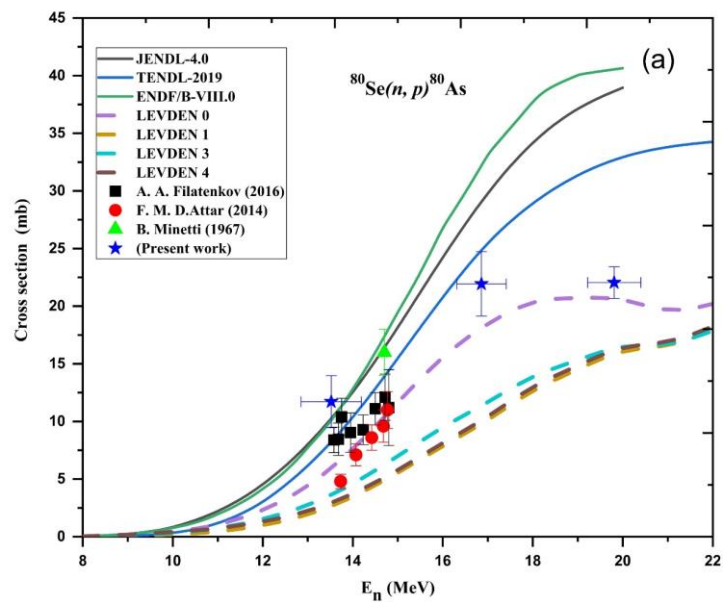


Fig. 6.3. (a) and (b) Comparison of the $^{78}\text{Se}(n,p)^{78}\text{As}$ reaction cross sections with literature data form EXFOR compilation, with JENDL, TENDL and ENDF evaluated libraries and with the theoretical results obtained from EMPIRE and TALYS codes.

6.3.1.4 The $^{80}\text{Se}(n,p)^{80}\text{As}$ excitation function

The measured cross section for the $^{80}\text{Se}(n,p)^{80}\text{As}$ reaction with their uncertainties are presented in Table 3.8 [Chapter 3]. The theoretical estimate of $^{80}\text{Se}(n,p)^{80}\text{As}$ reaction cross

section have been performed by EMPIRE code with different level density and nucleon potential as well as by TALYS code with ldmodel 1 to 6 along with the nucleon potential by considering exciton model preeqmode 2. The cross sections of $^{80}\text{Se}(n,p)^{80}\text{As}$ reaction discussed and compared with the theoretical data obtained from EMPIRE and TALYS codes, evaluated data of JENDL-4.0, TENDL-2019 and ENDF/B-VIII.0 libraries as well as with the literature data taken from EXFOR compilation as shown in Fig. 6.4. The large difference between JENDL-4.0, TENDL-2019 and ENDF/B-VIII.0 evaluated data are observed at above 14 MeV energy region. Our results at 13.52 MeV agrees with the existing data of A. A. Filatenkov [50] within the experimental uncertainties and with evaluated data of JENDL-4.0 and ENDF/B-VIII.0 libraries. Our data above 15 MeV are the first data in this energy range for the $^{80}\text{Se}(n,p)^{80}\text{As}$ reaction. We note that measured data at 16.86 MeV somewhere between the evaluated data of TENDL-2019 library and theoretical values of EMPIRE code using LEVDEN 0 as shown in Fig. 6.4(a). The present experimental result at higher energy 19.81 MeV agrees well with the theoretical data obtained from TALYS with ldmodel 1, 4, 5 and 6 level density model calculation as shown in Fig. 6.4(b).



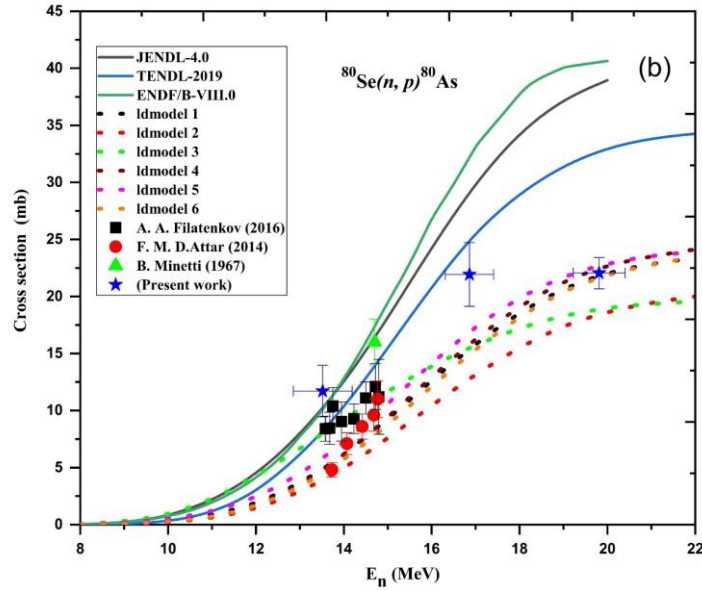


Fig. 6.4. (a) and (b) Comparison of the $^{80}\text{Se}(n,p)^{80}\text{As}$ reaction cross section with literature data from EXFOR compilation, JENDL, TENDL and ENDF evaluated libraries and with the theoretical results obtained from EMPIRE and TALYS codes.

6.3.2 The $^{65}\text{Cu}(n,p)^{65}\text{Ni}$ excitation function

The cross sections of the $^{65}\text{Cu}(n,p)^{65}\text{Ni}$ reaction at 13.52, 16.86, and 19.89 MeV neutron energies as measured in the present paper along with their uncertainties are given in Table 3.9 [Chapter 3]. Theoretical calculations were performed using the TALYS and EMPIRE codes, first with a default parameter and then with possible parameter adjustments. The present results were compared with the statistical model calculations, the latest evaluations, and the data from the previous measurements. Both theoretical codes included several OMPs, NLDs, PEs and γ SFs models as listed in Table 6.2.

Table 6.3 Summary of the $^{65}\text{Cu}(n,p)^{65}\text{Ni}$ reaction cross sections from the previous measurements.

Sample form	Decay data	Detector	Monitor reaction	Neutron source	Reference
Cu metal sheet	$E_\gamma=1481.84$, $I_\gamma=23.59$ $\tau_{1/2}=2.5175$ h	HPGe (30% relative efficiency)	$^{27}\text{Al}(n,\alpha)^{24}\text{Na}$	T(d, n) ^4He	A. Gandhi [57]
Cu Metal	$E_\gamma=1115.5$, $I_\gamma=15.43$ $\tau_{1/2}=2.5175$ h	HPGe (24.7% relative efficiency)	$^{93}\text{Nb}(n,2n)^{92m}\text{Nb}$	T(d, n) ^4He	A. A. Filatenkov [58]
CuO	$E_\gamma=1481.8$,	HPGe	$^{115}\text{In}(n,n')^{115m}\text{In}$	D(d, n) ^3He	Masataka

	$I_\gamma=23.59$ $\tau_{1/2}=2.5175$ h				Furuta [59]
Cu	$E_\gamma=1481.8$, $I_\gamma=23.59$ $\tau_{1/2}=2.5172$ h	HPGe (70% efficiency)	$^{27}\text{Al}(n, \alpha)^{24}\text{Na}$	$\text{D}(d, n)^3\text{He}$	W. Mannhart [60]
CuO	$E_\gamma=1115.5$, $I_\gamma=15.2$ $\tau_{1/2}=2.52$ h	Ge(Li)	$^{27}\text{Al}(n, \alpha)^{24}\text{Na}$	$\text{T}(d, n)^4\text{He}$	A. K. M. Harun [61]
CuO	$E_\gamma=1481.8$, $I_\gamma=23.59$ $\tau_{1/2}=2.5175$ h	HPGe (22% efficiency)	$^{115}\text{In}(n, n')^{115\text{m}}\text{In}$	$\text{D}(d, n)^3\text{He}$	T. Shimizu [62]
Cu Metal	$E_\gamma=1481.8$, $I_\gamma=23.59$ $\tau_{1/2}=2.5175$ h	Germanium intrinsic detector	$^{27}\text{Al}(n, \alpha)^{24}\text{Na}$	$^9\text{Be}(p, n)$	Yoshitomo Uwamino [71]
Cu	$E_\gamma=1115.84$ $I_\gamma=15.134$ $\tau_{1/2}=2.52$ h	Ge(Li)	$^{27}\text{Al}(n, \alpha)^{24}\text{Na}$	$\text{T}(d, n)^4\text{He}$	Y. Ikeda [64]
Cu	$E_\gamma=1481$, $I_\gamma=23.59$ $\tau_{1/2}=2.56$ h	Ge(Li)	$^{27}\text{Al}(n, \alpha)^{24}\text{Na}$	$\text{T}(d, n)^4\text{He}$	P. N. Ngoc [65]
Cu	$E_\gamma=1481.8$, $I_\gamma=23.59$ $\tau_{1/2}=2.5175$ h	Sodium-Iodide crystal	$^{56}\text{Fe}(n, p)^{56}\text{Mn}$	$\text{T}(d, n)^4\text{He}$	T. B. Ryves [66]
Cu	$E_\gamma=1482$ $I_\gamma=23.5$ $\tau_{1/2}=2.52$ h	Ge(Li)	$^{27}\text{Al}(n, \alpha)^{24}\text{Na}$	$\text{T}(d, n)^4\text{He}$	N. I. Molla [63]
Cu	$E_\gamma=1115$, $I_\gamma=16$ $\tau_{1/2}=2.564$ h	Sodium-Iodide crystal	$^{65}\text{Cu}(n, 2n)^{64}\text{Cu}$	$\text{T}(d, n)^4\text{He}$	G. N. Maslov [67]
Cu	$E_\gamma=1483$, $I_\gamma=25$ $\tau_{1/2}=2.55$ h	Ge(Li)	$^{56}\text{Fe}(n, p)^{56}\text{Mn}$	$\text{T}(d, n)^4\text{He}$	I. G. Clator [68]
Cu	$E_\gamma=1490$, $I_\gamma=23.59$ $\tau_{1/2}=2.56$ h	Sodium-Iodide crystal	$^{32}\text{S}(n, p)^{32}\text{P}$	$\text{T}(p, n)$ $\text{D}(d, n)^3\text{He}$ $\text{T}(d, n)^4\text{He}$	D. C. Santry [69]
Cu	$E_\gamma=1490$, $I_\gamma=25$ $\tau_{1/2}=2.6$ h	Boric acid counter	$^{27}\text{Al}(n, \alpha)^{24}\text{Na}$	$\text{T}(d, n)^4\text{He}$	M. Bormann [70]

6.3.2.1 Comparison of experimental and evaluation data

The present measurement of the $^{65}\text{Cu}(n,p)^{65}\text{Ni}$ reaction cross section is shown in Fig. 6.5 along with the literature data taken from the EXFOR compilation [10] and the evaluated data from ENDF/B-VIII.0, JEFF-3.3, JENDL-4.0/HE, CENDL-3.2, TENDL-2019 and FENDL-3.2 libraries [11-13,17-19] within the reaction threshold to 21 MeV neutron energy. Several authors studied the (n,p) reaction cross section of the ^{65}Cu isotope as mentioned in Table 6.3. As can be seen from Fig. 6.5, several measurements are available between 12 to 15 MeV and the results of the present measurements are consistent with the experimental and evaluation data. The measurements of Ryves *et al.* [66], Maslov *et al.* [67] and Santry *et al.* [69] were carried out by the NaI(Tl) detector to determine the $^{65}\text{Cu}(n,p)^{65}\text{Ni}$ reaction cross sections. The measured cross section of Maslov *et al.* [67] is much higher than those of the six evaluated excitation curves.

However, the reaction cross section predicted by Santry *et al.* [69] is varied over the entire energy region. Further, as can be seen, those recent measurements by Gandhi *et al.* [57] follow the trend of Uwamino *et al.* [71], Santry *et al.* [69] and Bormann *et al.* [70]. Our measured cross sections in the present paper at the neutron energies of 13.52, 16.86, and 19.89 MeV agree with the results of Santry *et al.* [69] within the experimental uncertainties. At the neutron energies above 19 MeV, only one measured datum is available and the present paper's result at 19.89 MeV is the second experimental evidence for the excitation curve of this cross section. Our result at 19.89 MeV can be compared with the data of Uwamino *et al.* [71]. As shown in Fig. 6.5, the reported Grimes *et al.* [72] cross section at 14.8 MeV is higher than the experimental data taken from the EXFOR database [10] and evaluated data of different libraries [11-13,17-19]. It is observed that the total proton production cross section is the sum of (n,p) , (n,np) and other reactions channels and therefore the value of the Grimes *et al.* cross section is higher compared to the activation cross section [57–71].

In addition, the existing experimental data and the evaluated data of the ENDF/B-VIII.0, JEFF-3.3, JENDL-4.0/HE, CENDL-3.2, TENDL-2019 and FENDL-3.2 libraries from threshold to 10 MeV are in good agreement with each other except the evaluation of the TENDL-2019 library, which shows a lower value of the cross section above the 10 MeV. However, the ENDF/B-VIII.0, JEFF-3.3, JENDL-4.0/HE, CENDL-3.2, TENDL-2019 and FENDL-3.2 libraries above 13 MeV show that the evaluated cross section differs largely in magnitude at the higher energy region. The cross section from the JENDL-4.0/HE library at

higher energies is 50 to 82% higher than the TENDL-2019 evaluation. The evaluated data of the CENDL-3.2 library are in excellent agreement with the present three data points at 13.52, 16.86 and 19.89 MeV neutron energies. In contrast, the evaluated data from the TENDL-2019 library are in excellent agreement with the present measurement at only 19.89 MeV. The latest evaluated data from the JENDL-4.0/HE library are in poor agreement with the present data and with the available experimental results above 15 MeV.

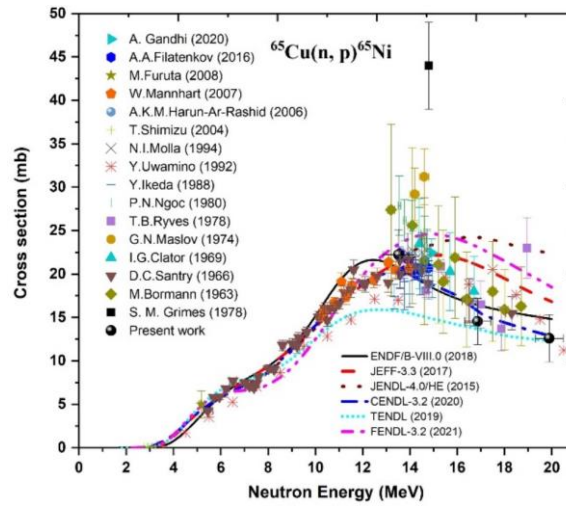


Fig. 6.5. Comparison of the present data with the previous measurements taken from the EXFOR compilation, data of S. M. Grimes et al. and the evaluated data from the ENDF/B-VIII.0, JEFF-3.3, JENDL-4.0/HE, CENDL-3.2, TENDL-2019 and FENDL-3.2 libraries.

6.3.2.2 Comparison of the experimental data with the theoretical values based on the TALYS and EMPIRE codes using default and adjusted parameters

The statistical model calculations using the TALYS and EMPIRE codes based on the phenomenological and microscopic level density models, first with a default parameter set and then with possible parameter adjustments, were performed and results are plotted in Figs. 6.6 and 6.7. The present and previous measurements were used to validate the theoretical calculations, taking into account the various optical potential, level density, and preequilibrium models provided by both codes.

Initially, the default TALYS results for the $^{65}\text{Cu}(n,p)^{65}\text{Ni}$ reaction cross section adopting the phenomenological and microscopic level density models are plotted in Figs. 6.6(a) and 6.6(b). The default theoretical calculations were performed for all level density

models along with the Koning-Delaroche local optical potentials and Kopecky-Uhl generalized Lorentzian E1 γ -ray strength function. As can be seen from Fig. 6.6(a), the constant temperature model performs very well for the present paper at 13.52, and for the data reported by A. Filatenkov [58], W. Mannhart *et al.* [60], and D. C. Santry *et al.* [69]. In contrast, the theoretical values based on the back-shifted Fermi gas and generalized superfluid models agree with the literature data at near threshold energies. Less satisfactory performance is noticed for the generalized superfluid and back-shifted Fermi gas models in the energy region between 6 and 25 MeV. From Fig. 6.6(b), the calculation with the default option based on the microscopic level density models Goriely, Goriely-Hilaire and Goriely-Hilaire Gogny diverges from the present and previous measurements at 7 to 25 MeV. The default theoretical results of all phenomenological and microscopic level density models failed to reproduce the excitation function from the threshold to 25 MeV.

Similarly, the default EMPIRE results of the $^{65}\text{Cu}(n,p)^{65}\text{Ni}$ reaction cross section adopting the phenomenological and microscopic level density models are plotted in Figs. 6.6(c) and 6.6(d). The default theoretical calculations were performed for all level density models along with the Koning-Delaroche optical potentials, exciton preequilibrium model (PCROSS) and modified Lorentzian γ -ray strength function (MLO1). The calculations from the EMPIRE code using the phenomenological level density models are shown in Fig. 6.6(c). These phenomenological calculations reproduced the cross sections from threshold to 8 MeV but failed to reproduce the excitation curve above 8 MeV. Furthermore, the excitation curve of the parity dependent HFM microscopic level density model is less satisfied with the present and previous measurements as shown in Fig. 6.6(d). The theoretical results from EMPIRE with the default option using the phenomenological and microscopic level density models failed to reproduce cross sections from threshold to 25 MeV.

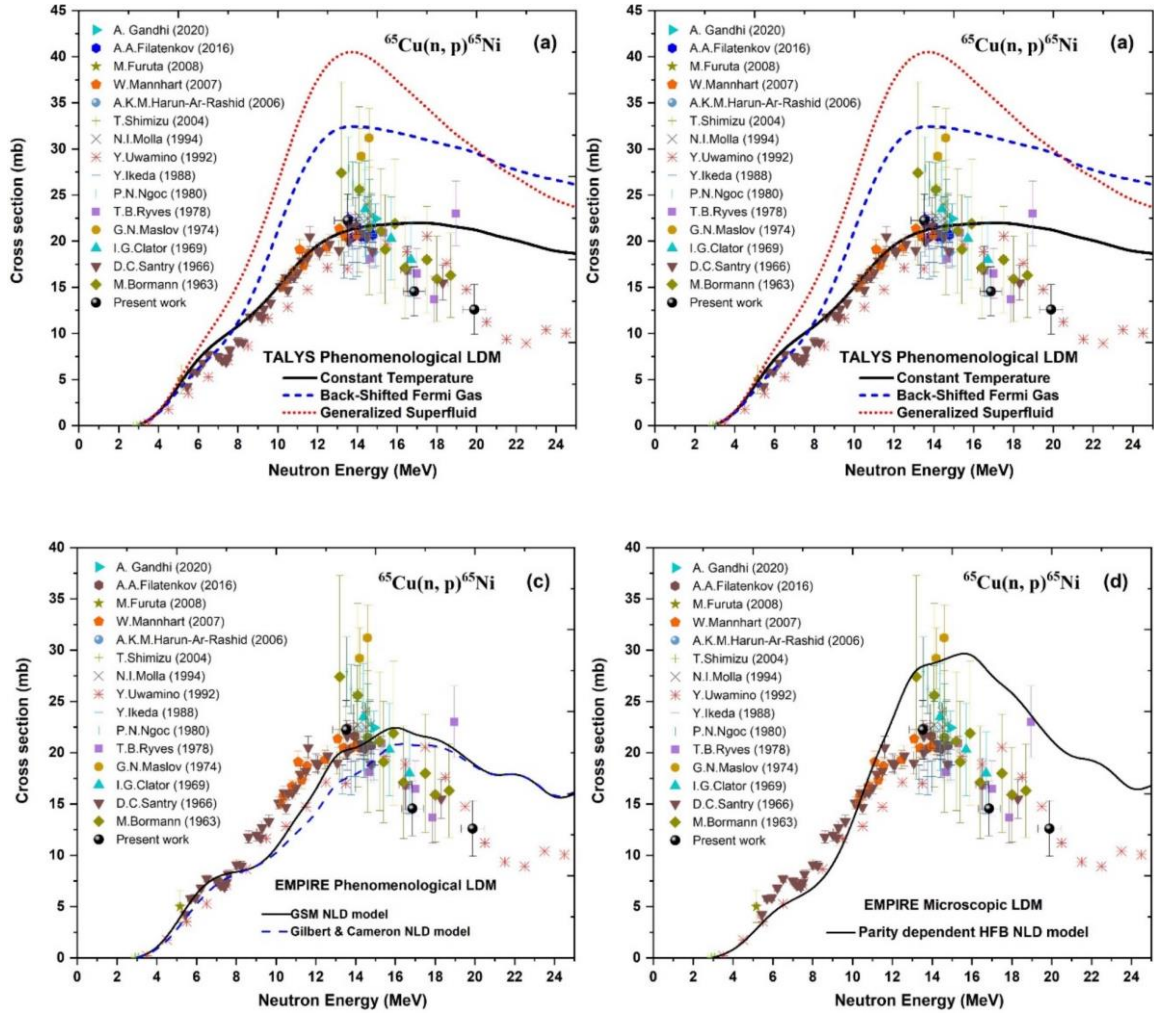


Fig. 6.6. The present $^{65}\text{Cu}(n, p)^{65}\text{Ni}$ reaction cross section along with the experimental data and theoretical values based on the (a)-(b) TALYS (ver. 1.9) and (c)-(d) EMPIRE (ver. 3.2.3) codes with the default option.

In view of large discrepancies between the measured cross section and the results from the statistical model codes TALYS and EMPIRE, using default parameters for the $^{65}\text{Cu}(n, p)^{65}\text{Ni}$ reaction, the theoretical values were revised with adjusted parameters to reproduce the experimental data more accurately. The optical potential, level density, and preequilibrium models and level-density parameters are of primary importance and have been individually adjusted to produce the previous and the present measured data. The adjusted values of the parameters and the adopted models to reproduce the measured data with statistical TALYS and EMPIRE codes are given in Tables 6.4 and 6.5. The theoretical results of modified calculations with adjusted level density parameters and models are illustrated in Fig. 6.7.

In TALYS calculations Figs. 6.7(a) and 6.7(b) the full j-l coupling was considered in the Hauser-Feshbach theory (TALYS keyword: “fullhf”) to improve the experimental cross section. The Hofmann-Richert-Tepel-Weidenmüller model for width fluctuation corrections in compound nucleus calculations is considered in the TALYS calculations. The behaviour of the constant temperature model was improved by combining the Koning-Delaroche local potential model with preequilibrium model 3 and widthmode 2. The parameters “asys” and “gshell” were enabled for this model to reproduce the experimental data. The excitation curve of the back-shifted Fermi gas model was improved by combining the optical potential of Koning-Delaroche global potential and the Kopecky and Uhl model for the γ -ray strength functions with widthmode 2. Furthermore, the theoretical calculations were improved when the generalized superfluid model was applied in combination with the optical potential of Koning-Delaroche global potential and the Kopecky and Uhl model for the γ -ray strength functions with widthmode 2. In addition, all microscopic level density models have better behaviour when combined with the Koning-Delaroche global potential and preequilibrium model 3 and widthmode 2 and taking “ctable” and “ptable” values. The value of the constant c (ctable) and δ (ptable) of the adjustment function for tabulated microscopic level densities were taken from the RIPL-3 database. In the theoretical calculations based on TALYS with default option consider these parameter values zero.

Table 6.4 The TALYS (ver. 1.9) adjusted model calculations with different statistical models and parameters of the $^{65}\text{Cu}(n, p)^{65}\text{Ni}$ reaction cross section.

Optical potential model	Level density models	Pre-equilibrium model	Widthmode	Parameters
Koning-Delaroche local	Constant temperature	preeqmode 3	2	asys y gshell y a 28 65 10.999
Koning-Delaroche dispersive	Back-shifted Fermi gas	preeqmode 3	2	asys y deltaW 28 65 1.1
Koning-Delaroche global	Generalized superfluid	preeqmode 3	2	asys y deltaW 28 65 1.61

Koning-Delaroche global	S. Goriely	preeqmode 3	2	ptable 28 65 1.123
Koning-Delaroche global	S. Goriely-S. Hilaire	preeqmode 3	2	ctable 28 65 0.705 ptable 28 65 0.833
Koning-Delaroche global	S. Goriely-S. Hilaire Gogny force	preeqmode 3	2	asys y gshell y ctable 28 65 0.705 ptable 28 65 0.833

Table 6.5 The EMPIRE (ver. 3.2.3) adjusted model calculations with different statistical models and parameters of the $^{65}\text{Cu}(n,p)^{65}\text{Ni}$ reaction cross section.

Optical potential model	Level density models	Pre-equilibrium model	γ -ray strength function model	Parameters
Koning-Delaroche	Generalized superfluid	Multi-Step-Compound (MSC)	Standard Lorentzian (SLO)	ATILNO 0.96 GDIV 8.0 STMRO 2.0 GTILNO 1.1 PCROSS 1.18
	Gilbert-Cameron	Exciton model (PCROSS)	Modified Lorentzian (MLO1)	PCROSS 0.8 ATILNO 0.9 GCROT 1.35
	Hartree-Fock-BCS (HF-BCS)	Multi-Step-Compound (MSC)	Modified Lorentzian (MLO1)	ROHFBP 0.7 GDIV 5.0

The EMPIRE code was also used to do theoretical calculations, using alternative models for optical model parameterization, level density, and γ -ray strength functions. The adjusted theoretical calculation based on the phenomenological models is shown in Fig. 6.7(c). This calculation reproduced the previous and present work by considering the different models and parameters as mentioned in Table 6.5. Similarly, the microscopic calculation based on the parity dependent HFM models was improved by combining and adjusting the values of parameters in theoretical calculations as shown in Fig. 6.7(d). The reduction in the preequilibrium emission contribution and adjusting the values of the parameters resulted in a more accurate reproduction of the experimental results over the whole energy range.

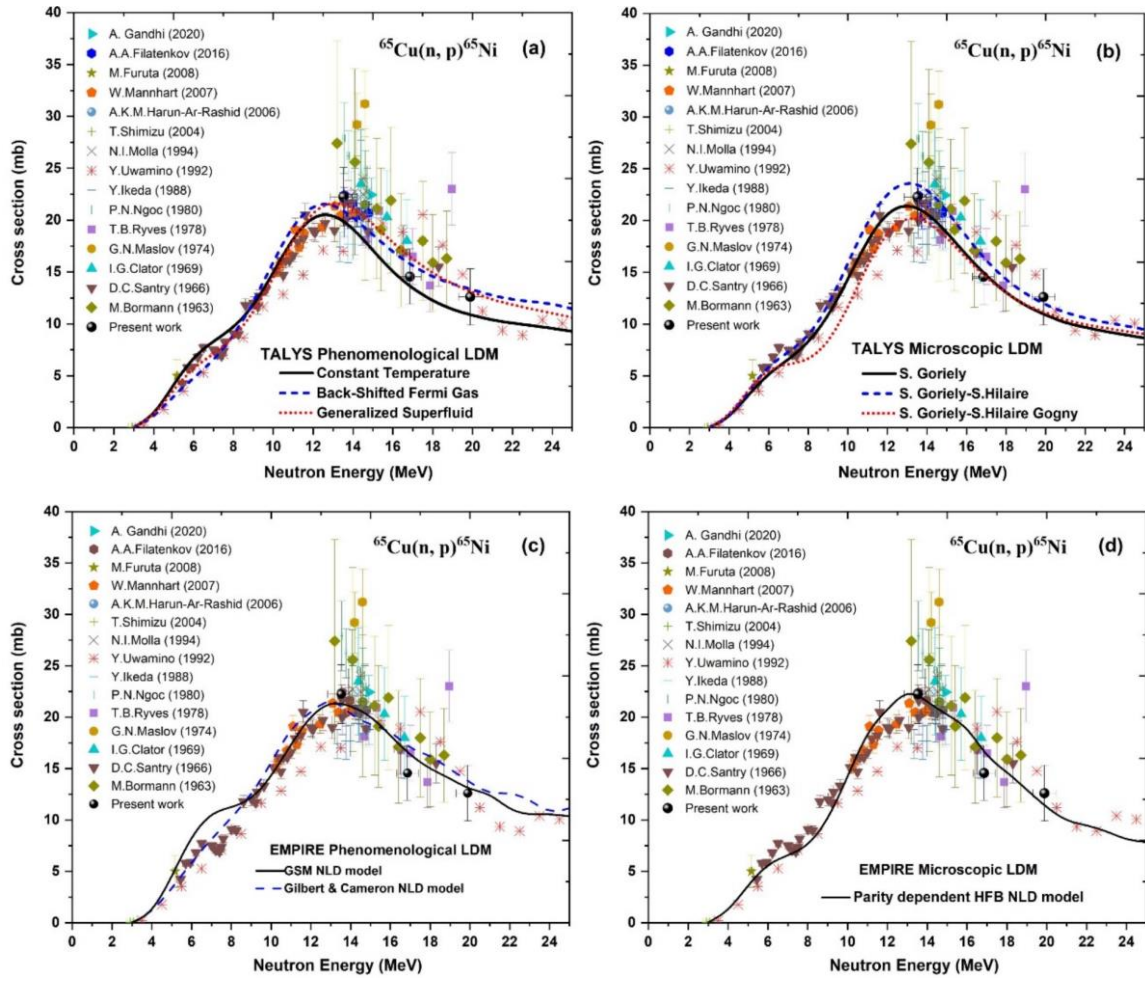


Fig. 6.7. The present $^{65}\text{Cu}(n, p)^{65}\text{Ni}$ reaction cross section along with the experimental data and adjusted theoretical values obtained from the (a)-(b) TALYS (ver. 1.9) and (c)-(d) EMPIRE (ver. 3.2.3) codes with adjusted parameters.

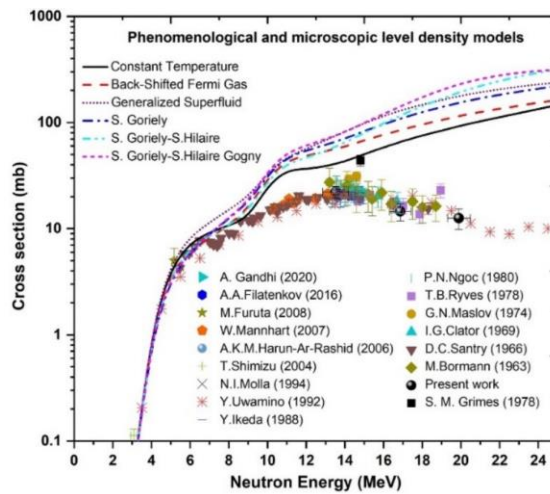


Fig. 6.8. Comparison of the activation cross section [7-21] and total proton emission cross sections [22] with the theoretical calculations performed by the TALYS (ver. 1.9) code.

In addition, the theoretical calculations were performed to reproduce the data of Grimes *et al.* at 14.8 MeV using the TALYS code based on the phenomenological and microscopic level density models. The total proton production cross-section data of Grimes *et al.* [72] are reproduced by the default calculation based on the phenomenological constant temperature model as shown in Fig. 6.8. Moreover, the back-shifted Fermi gas and generalized superfluid phenomenological and three microscopic level density models predict higher value of the cross section.

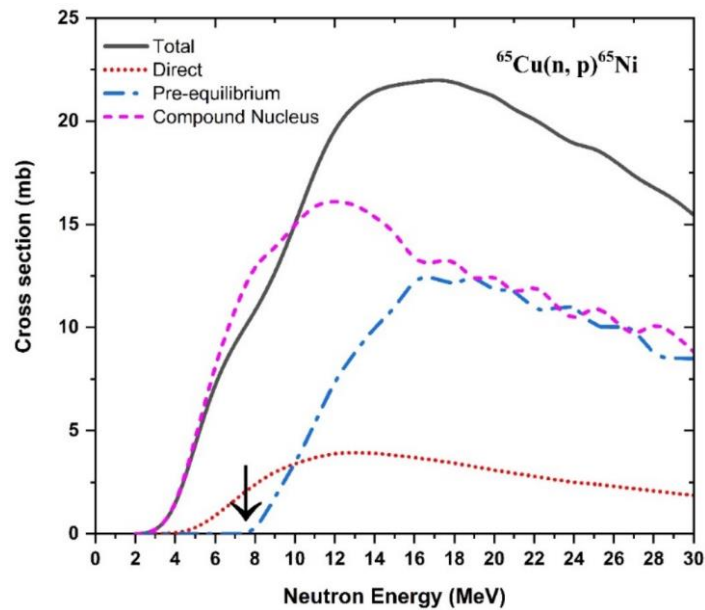


Fig. 6.9. The contribution of the cross section in $^{65}\text{Cu}(n, p)^{65}\text{Ni}$ reaction from different reaction processes (direct, pre-equilibrium and compound) to the total reaction cross section was calculated using the TALYS (ver. 1.9) code.

At higher neutron energies the cross-section measurements are also interesting since the contribution of the preequilibrium mechanism to the total reaction cross section becomes important. The present measurements extend above 15 MeV incident neutron energy, and the preequilibrium processes are expected to assume significance at energies above 10 MeV. The various theoretical preequilibrium models were considered to describe a cross section of the $^{65}\text{Cu}(n, p)^{65}\text{Ni}$ reaction at higher neutron energies. TALYS uses the exciton model based on numerical transition rates with an energy-dependent matrix element as the default choice for the preequilibrium reactions. In the present paper, the contribution of different reaction mechanisms (compound, preequilibrium, and direct) to the total reaction cross section of the $^{65}\text{Cu}(n, p)^{65}\text{Ni}$ reaction was calculated by the TALYS code. The dominance of each reaction mechanism is illustrated in Fig. 6.9. As can be seen, the compound and preequilibrium

mechanisms are a significant portion of reaction cross sections. Above the 8 MeV neutron energy, the contribution of the preequilibrium emission increases with energy. Equally, it contributes to the present reaction cross section from the compound nucleus process with a minor contribution from the direct reaction.

6.3.3 The $^{52}\text{Cr}(n, p)^{52}\text{V}$ excitation function

The excitation function for the $^{52}\text{Cr}(n, p)^{52}\text{V}$ reaction along with the experimental [73-82] and latest evaluated data [6-10] is shown in Fig. 6.10. Below 9 MeV neutron energy W. Mannhart *et al.* [74] and D. L. Smith *et al.* [80] reported the measured cross sections. In this region, there are no contributions from the $^{53}\text{Cr}(n, np)^{52}\text{V}$ and $^{53}\text{Cr}(n, d)^{52}\text{V}$ reactions since the reaction threshold energies are 11.34 and 9.07 MeV, respectively. Hence measurements carried out using a natural sample of chromium give a pure $^{52}\text{Cr}(n, p)^{52}\text{V}$ reaction cross section.

As shown in Fig. 6.10, the measured cross sections of W. Mannhart *et al.* [74], A. Fessler *et al.* [75] and D. L. Smith *et al.* [80] agree very well with the FENDL-3.2b and CENDL-3.2 evaluation and are in fair agreement with TENDL-2019, ENDF-B/VIII.0 and JENDL-5.0 libraries. It is worth mentioning that at around 14–15 MeV neutron energy where multiple measured data are available, the data agree with each other within 10%, whereas the data from S. K. Ghorai *et al.* [78], I. G. Clator [81] and B. D. Kern *et al.* [82] are either too high or too low and there is no consistent agreement among them. Above 14 MeV incident neutron energy, all the measured cross sections show different values above or below the evaluated cross section data. The measured data by S. K. Ghorai *et al.* [78] around 14 MeV deviate too much from all existing measured cross sections, and the true excitation curve does not seem to follow the trend of this data set, because measured data below 12 MeV neutron energy are quite accurate and the contribution from the $^{53}\text{Cr}(n, x)^{52}\text{V}$ reaction is zero or negligibly small.

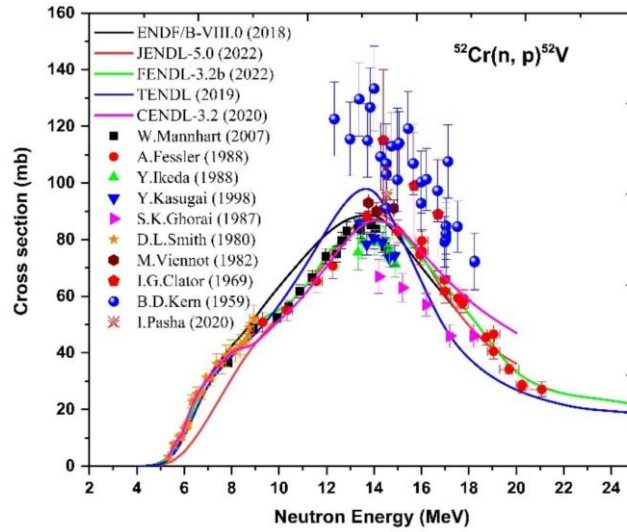


Fig. 6.10. Literature cross sections compared with the latest evaluated data libraries.

The obtained theoretical results from the TALYS code based on the phenomenological and microscopic level density models are presented in Figs. 6.11(a-d). For all these calculations, various phenomenological and microscopic level density models were parameterized as given in Table 6.6. The theoretical cross section of $^{52}\text{Cr}(n, p)^{52}\text{V}$ reaction was compared with previous results of Ref. [73-82]. The theoretical trends presented in Fig. 6.11(a), are based on the phenomenological model of the level densities. The calculation, which uses the optical model of Koning and Delaroche and the modified Lorentzian model for the γ -ray strength functions, reproduces the previous results at lower energies and the high energy part of the excitation function. A comparison with the model calculation shows that in the energy range of 11 to 20 MeV, the constant temperature model systematically underestimates the experimental data. The Koning and Delaroche optical potential and the Kopecky and Uhl γ -strength functions allow better data reproduction at the near-threshold energies. Above 15 MeV, the data by S. K. Ghorai *et al.* [78] agree with the calculated values from the TALYS code. However, the reported data by B. D. Kern *et al.* [82] within the neutron energies of 12–20 MeV are systematically higher than the data of literature and theoretical values from the TALYS code.

Table 6.6 Theoretical models and optimum parameters are used in TALYS calculations to reproduce the data of ^{52}Cr isotope.

^{52}Cr	Constant temperature	preeqmode 1	jlmomp y	alphald 0.06326 betald 0.2728 widthmode 0 strength 1	Fullhf
	Back-shifted Fermi gas	preeqmode 1	dispersion y	alphald 0.06426 betald 0.19531 gammald 0.051	fullhf
	Generalized superfluid	preeqmode 2	jlmomp y	alphald 0.1226 betald 0.03536	Fullhf asys
	S. Goriely	preeqmode 1	jlmomp y	ctable -0.1005 ptable -0.20419 a 11.22 strength 1 widthmode 2	fullhf gshell
	S. Goriely-S. Hilaire	preeqmode 2	localomp	ctable 0.1650 ptable -0.20419 deltaW -0.61442 pairconstant 10.3	Fullhf
	S. Goriely-S. Hilaire Gogny force	preeqmode 2	localomp n	ctable 0.1005 ptable -0.20419 preeqspin 3 deltaW 0.6142 pair 3.124	Fullhf gshell

In Fig. 6.11(b), the theoretical calculations resulting from the TALYS code are presented, but this time using three microscopic models for the level density calculations. Among these, the model described by Goriely *et al.* (microscopic model 2) exhibits the best behaviour since it accurately describes the energy areas examined in the earlier measurements. The data reproduction of the Goriely *et al.* (microscopic model 1) microscopic model is also quite good. The behaviour of the microscopic model was improved by combining it with the semi-microscopic optical potential of the Bauge *et al.* exciton pre-equilibrium model and a microscopic model for the strength functions based on Hartree-Fock-Bogolyubov calculations as shown in Fig. 6.11(d). The resulting fit for the $^{52}\text{Cr}(n, p)$ reaction cross section is illustrated in Figs. 6.11(c-d). The level density parameters and the adjustments adapted to fit the experimental data using the TALYS code are given in Table 6.6. The theoretical excitation function of the (n, p) reaction for ^{52}Cr using adjustments is in

substantially better agreement with the literature data compared to the calculations with default parameters.

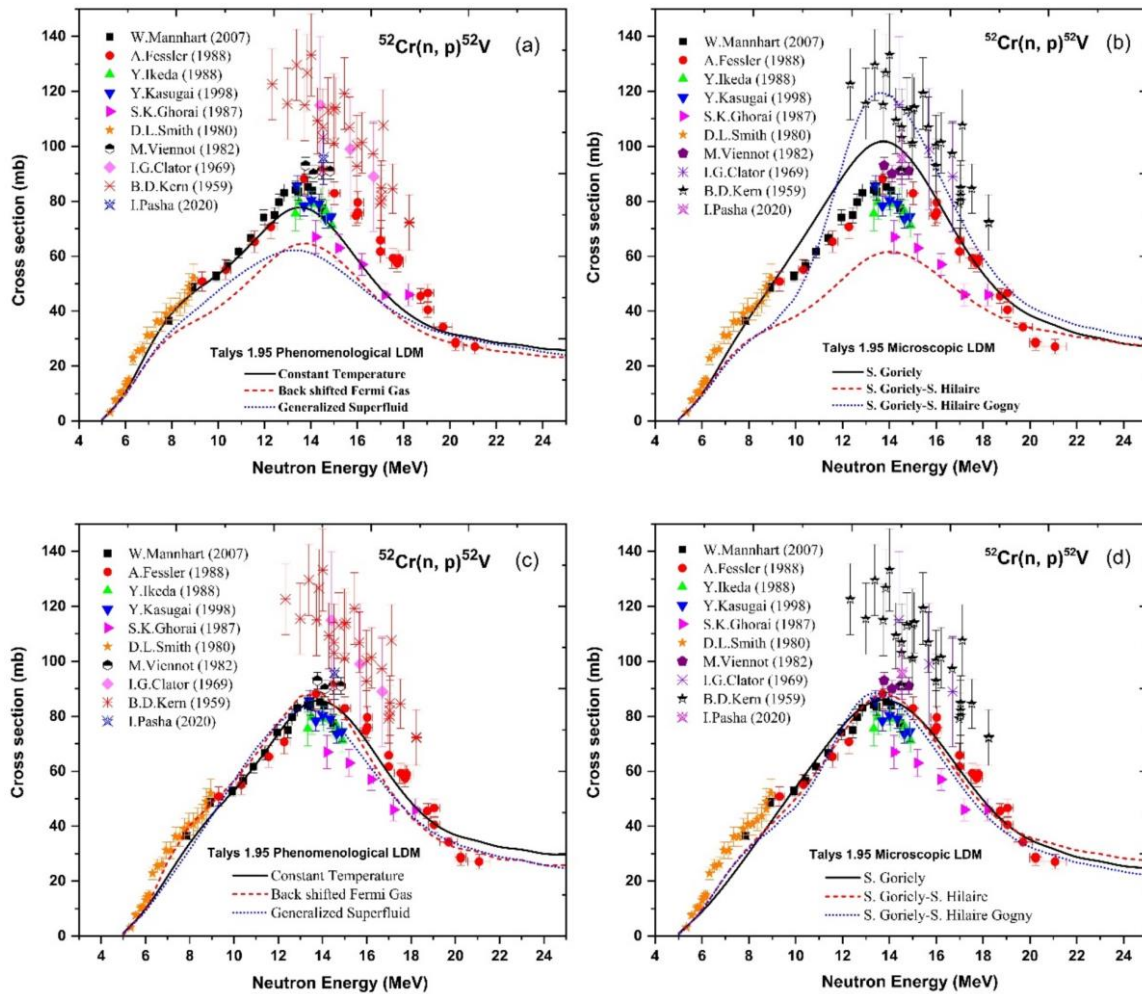


Fig. 6.11. Literature cross sections compared with the TALYS (ver. 1.95) calculations based on the phenomenological and microscopic level density models (a-b) Default (c-d) Adjusted.

6.3.4 The $^{51}\text{V}(n, p)^{51}\text{Ti}$ excitation function

The present measurements of the $^{51}\text{V}(n, p)^{51}\text{Ti}$ reaction cross section at three different neutron energies are given in Table 3.7 [Chapter 3]. The excitation function from neutron energies reaction threshold to 22 MeV is plotted in Fig. 6.12 along with the previous data and latest evaluations. The present measurements of the $^{51}\text{V}(n, p)^{51}\text{Ti}$ reaction was discussed and compared with literature data taken from the EXFOR compilation [10], evaluations of the ENDF/B-VIII.0, JENDL/AD-2017 and TENDL-2019 libraries [11,15,18] and theoretical calculations using statistical TALYS code.

As can be seen from Fig. 6.12, the present measurements at 7.87, 13.05 and 16.98 MeV energies are in excellent agreement with the results of W. Mannhart *et al.* [92], Y. Ikeda *et al.* [83], A. Fessler [84], and D. L. Smith *et al.* [85]. However, the measurements of Y. Uwamino *et al.* [90] are lower than the present work and available literature data except for the data of A. Fessler [84] above 19 MeV. The present measurements agree with the ENDF/B-VIII.0 and TENDL-2019 evaluations at all energies except the JENDL/AD-2017 evaluation at 16.98 MeV energy. In contrast, the cross section of the JENDL/AD-2017 data library underestimates the $^{51}\text{V}(n,p)^{51}\text{Ti}$ reaction cross section above 13 MeV and favor the higher energies experimental data of the Y. Uwamino *et al.* [90], P. Reimer *et al.* [93], Y. Ikeda *et al.* [83], K. Fang *et al.* [91] and W. Mannhart *et al.* [92]. At higher energies region the measurements of T. Katoh *et al.* [89] and M. Borman *et al.* [86] shows larger cross section values than the evaluations of JENDL/AD-2017, ENDF/B-VIII.0 and TENDL-2019 libraries. The previous measurements above 16 MeV are limited and demonstrate significant discrepancies. The measured data of A. Fessler [84] above 16 MeV is not favouring evaluations of the JENDL/AD-2017, ENDF/B-VIII.0 and TENDL-2019 libraries systematically as shown in Fig. 6.12 and agree with the data of Y. Uwamino *et al.* [90] within experimental uncertainties. In contrast, the data of A. Fessler [84] shows lower value of cross section compared to the data of Borman *et al.* [86] within 16-19 MeV energies. The evaluations cross sections of ENDF/B-VIII.0, JENDL/AD-2017 and TENDL-2019 libraries were obtained from the different code and models as described in the ref. [11,15,18]. The cross sections obtained from the evaluations of JENDL/AD-2017, ENDF/B-VIII.0 and TENDL-2019 libraries are in good agreement with each other from threshold to 14 MeV energies region, whereas at above 14 MeV the cross section of JENDL/AD-2017 libraries show lower values of cross section compared to the TENDL-2019 and ENDF/B-VIII.0 libraries as shown in Fig. 6.12.

Table 6.7 Cross section for $^{51}\text{V}(n,p)^{51}\text{Ti}$ reaction estimated over the threshold to 22 MeV neutron energies using different optical potential models of the TALYS code.

Optical potential models	Level density model	Pre-equilibrium model	$E1$ γ -ray strength function model
Koning-Delaroche local potential Koning-Delaroche global potential Koning-Delaroche local-dispersive potential Bauge-Delaroche JLM potential	Constant temperature model	Preeqmode 2	Kopecky-Uhl generalized Lorentzian

Table 6.8 Cross section for $^{51}\text{V}(n,p)^{51}\text{Ti}$ reaction estimated over the threshold to 22 MeV neutron energies using different pre-equilibrium models of the TALYS code.

Optical potential model	Level density model	Pre-equilibrium models	$E1$ γ -ray strength function model
Koning-Delaroche local potential	Constant temperature model	Preeqmode 1 Preeqmode 2 Preeqmode 3 Preeqmode 4	Kopecky-Uhl generalized Lorentzian

Table 6.9 Cross section for $^{51}\text{V}(n,p)^{51}\text{Ti}$ reaction estimated over the threshold to 22 MeV neutron energies using different level density options of the TALYS code.

Optical potential model	Level density models	Pre-equilibrium model	$E1$ γ -ray strength function model
Koning-Delaroche local potential	Constant temperature model Back-shifted Fermi Gas model Generalized Superfluid model S. Goriely microscopic model S. Goriely-S. Hilaire microscopic model S. Goriely-S. Hilaire Gogny force microscopic model	Preeqmode 2	Kopecky-Uhl generalized Lorentzian

Table 6.10 The default and adjust level density parameters of the $^{51}\text{V}(n,p)^{51}\text{Ti}$ reaction cross section.

level density models	Parameters	α	β	γ_1	γ_2	asys	gshell	pair	pair constant	Ntop	δW
ldmodel 1	Default	0.0692	0.2827	0.4331	0	n	n	-	-	-	-
	Adjustment	0.0371	0.4561	0.942	0	y	y	-	-	-	-
ldmodel 2	Default	0.0722396	0.195267	0.410289	0	n	n	-	-	16	-0.314
	Adjustment	0.068	0.489	0.323	0.132	n	y	-	-	29	-2.987
ldmodel 3	Default	0.110575	0.0313662	0.648723	0	n	n	-	12	-	0.452
	Adjustment	0.098	0.5	1.0	0.2	y	y	1.099	19.03	-	-0.897
ldmodel 4	Parameters	ptable			Pair						
	Default	0			-						
	Adjustment	1.543			-						
ldmodel 5	Default	0			-						
	Adjustment	1.26			-						
ldmodel 6	Default	0			-						
	Adjustment	1.99			0.981						

However, the evaluations of the ENDF/B-VIII.0 and TENDL-2019 libraries are agreed very well with each other from threshold to 22 MeV energies region and agree with experimental data of the A. Fessler [84] only at 17.03 MeV and present measurement at 16.98 MeV. The differences in evaluated cross sections are observed due to the parameters adjustment at higher energies. The present measurements at three different energies are helpful in the mapping of the excitation function over a broad energy region.

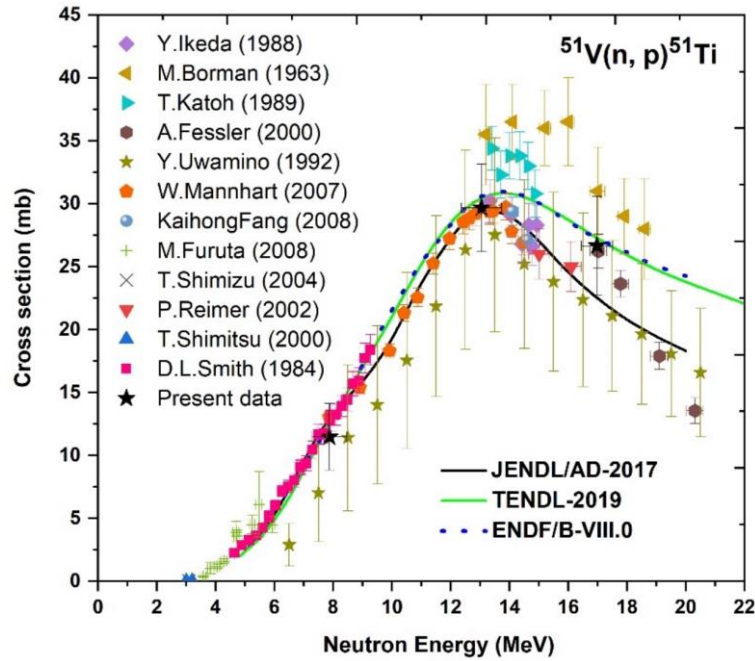


Fig. 6.12. The comparison of the measured $^{51}\text{V}(n, p)^{51}\text{Ti}$ reaction cross section and the experimental and JENDL/AD-2017, ENDF/B-VIII.0 and TENDL-2019 evaluation.

The different optical potential models along with the constant temperature level density and other models are given in Table 6.7. These models were used to calculate the $^{51}\text{V}(n, p)^{51}\text{Ti}$ reaction cross sections and theoretical results obtained from the TALYS code are plotted in Fig. 6.13(a). The cross sections are overestimated by the all-optical potential models within 7 to 13 MeV energies region and does not show agreement with the experimental and evaluations of the JENDL/AD-2017, ENDF/B-VIII.0 and TENDL-2019 libraries. In contrast, the KD local and dispersive potential shows good agreement with the present work at 13.05 and 16.98 MeV energies within experimental uncertainties, while evaluations of the TENDL-2019 and ENDF/B-VIII.0 libraries at higher energies shows agreement only with the KD local potential. However, the KD global and BD jlmomp optical potential models are overestimated the cross section compared to evaluations of the JENDL/AD-2017, ENDF/B-VIII.0 and TENDL-2019 libraries and show agreement with the measurement of T. Katoh *et al.* [89] within 13 to 15 MeV and M. Borman *et al.* [86] at above 16 MeV energies as shown in Fig. 6.13(a).

Furthermore, theoretical calculations were performed using the different pre-equilibrium models and constant temperature level density using the TALYS code as mentioned in Table 6.8, along with the other models. The cross sections obtained from the different pre-equilibrium models are plotted in Fig. 6.13(b) along with the experimental and evaluations of the JENDL/AD-2017, ENDF/B-VIII.0 and TENDL-2019 libraries. It is

observed from the theoretical calculations that above 10 MeV, the contribution in cross section is coming from the pre-equilibrium process. Therefore, different pre-equilibrium models were tested in the present work to explain the literature experimental and evaluations of the JENDL/AD-2017, ENDF/B-VIII.0 and TENDL-2019 libraries. The theoretical cross section estimated from the multi-step direct/compound model (preeqmode 4) was quite unsatisfied with experimental and evaluations, whereas the exciton model: Numerical transition rates with the optical model for collision probability (preeqmode 3) does not reproduce the present work, experimental and evaluated cross section above 11 MeV. In contrast, the exciton model: Analytical transition rates with energy-dependent matrix element (preeqmode 1) and exciton model: Numerical transition rates with energy-dependent matrix element (preeqmode 2) show good agreement with present work at 13.05 and 16.98 MeV within experimental uncertainties and overestimated the cross section within 6 to 12 MeV energies region with compared to experimental and evaluations data. The pre-equilibrium model 2 show agreement with the evaluations of the ENDF/B-VIII.0 and TENDL-2019 libraries, literature data of A. Fessler [84] at 16 MeV and data of T. Katoh *et al.* [89] within 13 to 15 MeV energies, whereas the pre-equilibrium model 1 show agreement with the experimental data of the M. Borman *et al.* [86] at higher energies as shown in Fig. 6.13(b).

Theoretical calculations with different phenomenological and microscopic level density models as mentioned in Table 6.9 along with the other models were performed from the threshold to 22 MeV energies and obtained results are plotted in Figs. 6.14(a) and 6.14(b). The cross section estimated from the first phenomenological constant temperature model (ldmodel 1) describes the data of M. Furuta *et al.* [87], D. L. Smith *et al.* [85], T. Shimizua *et al.* [88] from the threshold to 6 MeV energies and higher energies present data within experimental uncertainties. This theoretical level density model also describes the data of A. Fessler [84] as well as evaluations of the ENDF/B-VIII.0 and TENDL-2019 libraries from 14 to 22 MeV energies. In contrast, this model overestimates the cross section within 6 to 12 MeV energies. Further calculation from the second phenomenological back shifted Fermi gas level density model (ldmodel 2) reproduce the present work at 7.87 MeV energy, literature D. L. Smith *et al.* [85], and evaluations of the JENDL/AD-2017, ENDF/B-VIII.0 and TENDL-2019 libraries from the threshold to 9 MeV neutron energy range as shown in Fig. 6.14(a). In contrast, above 9 MeV energy the theoretical cross section from ldmodel 2 is very high and does not match with the experimental and evaluations. The statistical calculation with the third phenomenological generalized superfluid level density model (ldmodel 3) show good agreement with the lower energies data of M. Furuta *et al.* [87], whereas this model

overestimating the cross sections above 6 MeV energy and does not reproduce the experimental and evaluations of the JENDL/AD-2017, ENDF/B-VIII.0 and TENDL-2019 libraries.

The theoretical microscopic level density model S. Goriely (ldmodel 4) and S. Hilaire-S. Goriely calculation based on the Hartree-Fock model (ldmodel 5) describes the lower energy literature data from the threshold to 9 MeV energies, evaluations from the threshold to 6 MeV and high-energy experimental data of the M. Borman *et al.* [87] as shown in Fig. 6.14(b). The microscopic level density model S. Hilaire-S. Goriely Gogny based on the Temperature-dependent Hartree-Fock-Bogolyubov calculations (ldmodel 6) overestimate the cross sections of the present work at 7.87, 13.05 and 16.98 MeV energies, experimental and evaluations of the JENDL/AD-2017, ENDF/B-VIII.0 and TENDL-2019 libraries. However, it can be seen from Fig. 6.14(b) that theoretical calculations based on all three microscopic level density models do not reproduce all experimental data from the threshold to 22 MeV energies.

As can be seen from Fig. 6.14, theoretical calculations based on the different level density, optical potential and pre-equilibrium models with default input parameters does not reproduce the $^{51}\text{V}(n,p)^{51}\text{Ti}$ reaction cross section from the threshold to 22 MeV neutron energy range. These default theoretical calculations fail to show good agreement with experimental and evaluations of the JENDL/AD-2017, ENDF/B-VIII.0 and TENDL-2019 libraries. It indicates that theoretical calculations need input parameters adjustment to find better agreement with the experimental and evaluations from threshold to 22 MeV energies. The statistical model calculations were performed using the TALYS code with the pre-equilibrium model (preeqmode 2), optical KD local potential and with the six different phenomenological and microscopic level density models of the $^{51}\text{V}(n,p)^{51}\text{Ti}$ reaction cross section. In the present work, the different level density parameters were adjusted to reproduce the present measured cross section at all energies. The theoretical calculations obtained by using the modified input parameters of phenomenological and microscopic level density models show excellent agreement with present work at 7.87, 13.05 and 16.98 MeV neutron energies and the experimental data taken from the EXFOR database as shown in Figs. 6.15(a) and 6.15(b). The theoretical calculations with modified parameters were reproduced the evaluations of latest ENDF/B-VIII.0 and TENDL-2019 libraries. The values of different default and adjusted input parameters for phenomenological and microscopic level density models are given in Table 6.10. In the present work, the systematic effect of all parameters

from lower to higher energy region was studied to reproduce the $^{51}\text{V}(n, p)^{51}\text{Ti}$ reaction cross section of the present work. In $^{51}\text{V}(n, p)^{51}\text{Ti}$ reaction, the contribution of the cross section from various reaction processes is seen in Fig. 6.16, and it can be shown that the influence of pre-equilibrium emission increases with energy above 8 MeV. It similarly contributes to the present cross section as the compound nucleus process, with a small contribution from the direct reaction at the higher energies.

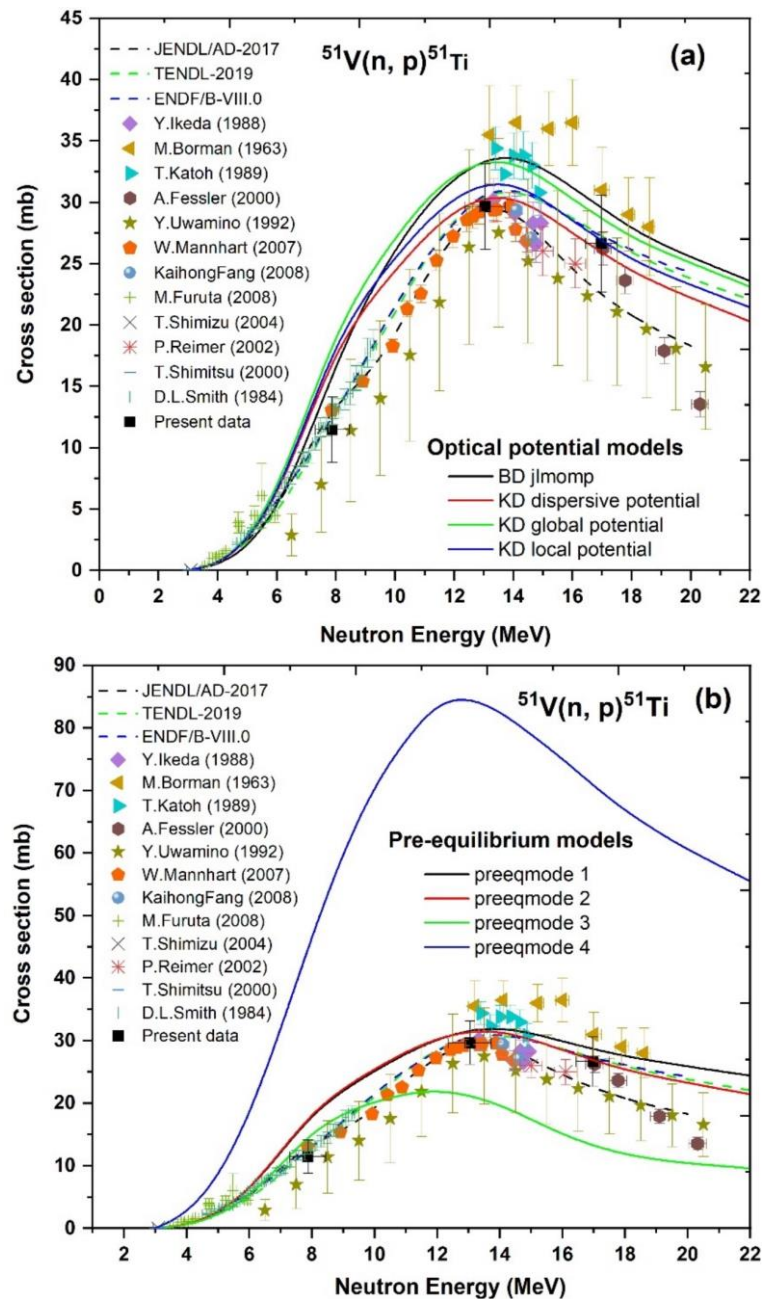


Fig. 6.13. The comparison of the measured $^{51}\text{V}(n, p)^{51}\text{Ti}$ reaction cross section with literature, evaluations and with the theoretical calculations using the statistical TALYS (ver. 1.9) code using different (a) optical potential models and (b) pre-equilibrium models.

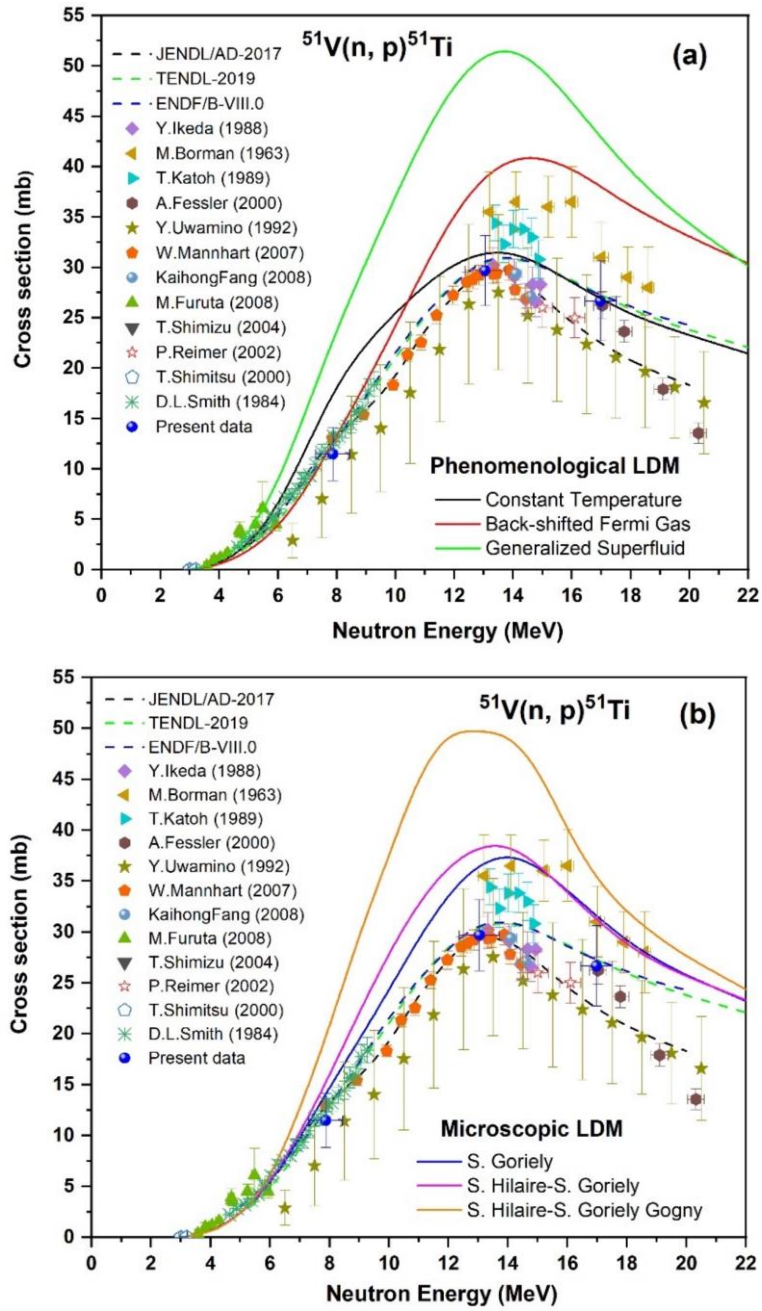


Fig. 6.14. The comparison of the $^{51}\text{V}(n, p)^{51}\text{Ti}$ reaction cross section with literature, evaluations and with the theoretical calculations using the statistical TALYS (ver. 1.9) code using different (a) Phenomenological and (b) Microscopic level density models.

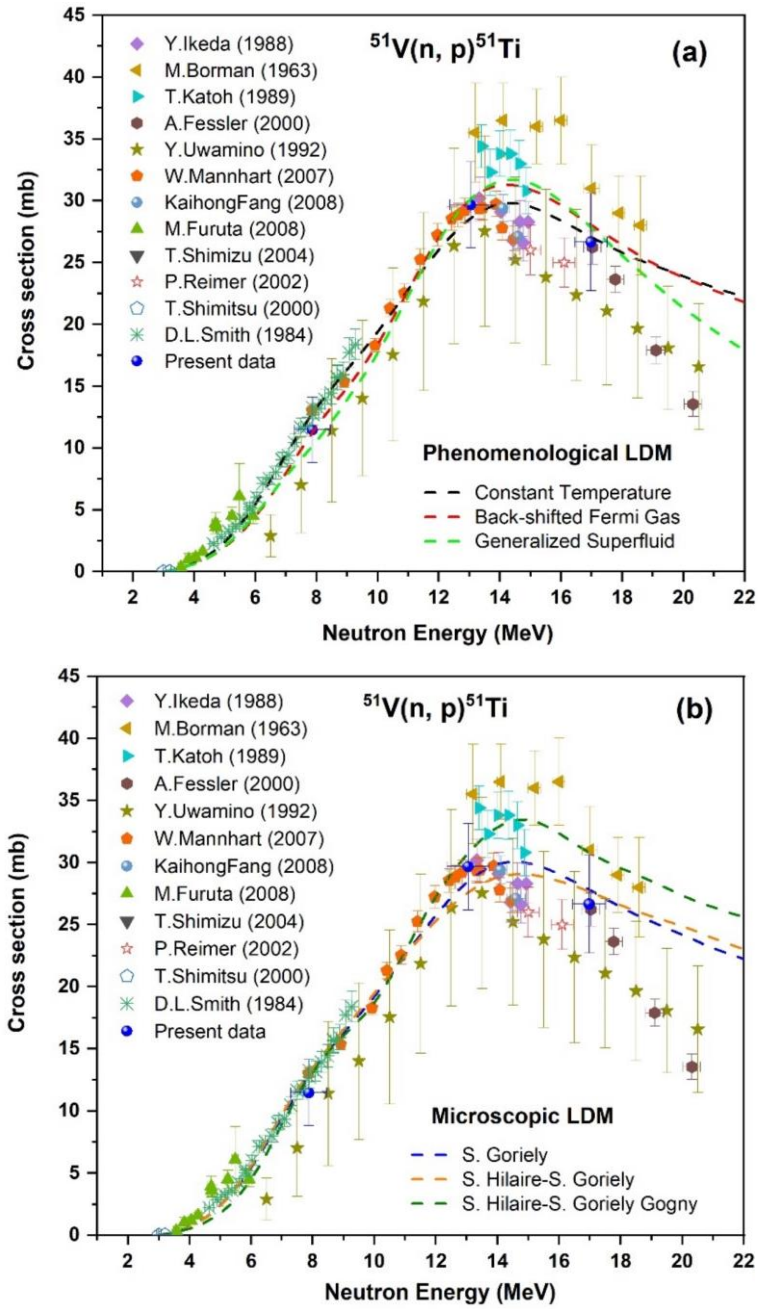


Fig. 6.15. The theoretical calculations of the $^{51}\text{V}(n, p)^{51}\text{Ti}$ reaction cross section as performed by the TALYS (ver. 1.9) code with the adjusted parameters of the (a) Phenomenological and (b) Microscopic level density models.

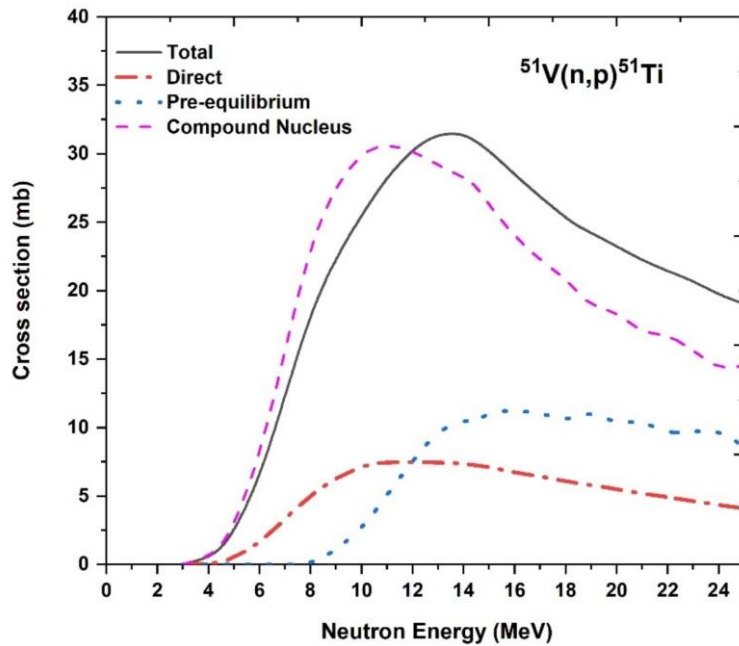


Fig. 6.16. The contribution of the different cross section in $^{51}\text{V}(n,p)^{51}\text{Ti}$ reaction.

6.3.5 The $^{48}\text{Ti}(n,p)^{48}\text{Sc}$ excitation function

The excitation function of the $^{48}\text{Ti}(n,p)^{48}\text{Sc}$ reaction along with the reported measured [94-107] and evaluated data libraries [16, 17, 18, 19] is shown in Fig. 6.17. A good agreement among literature data has been found within experimental uncertainties except with the few data, probably due to the use of old nuclear decay data and monitor values in those analyses. These reported cross sections were measured by many labs and there is a large discrepancy in the energy region of 13-16 MeV. Below 13 MeV, the $^{48}\text{Ti}(n,p)^{48}\text{Sc}$ reaction was studied in various previous measurements [94-107] and the latest TENDL-2019, FENDL-3.2b, JENDL-5.0 and CENDL-3.2 evaluation reproduces the previous experimental data well. The evaluation follows the measurements up to 13 MeV and is different in values above 13 MeV energies. At energies above 14 MeV, the latest evaluated data JENDL-5.0 is 10 % higher than the evaluated data of the CENDL-3.2 library. It's observed that the high energies data of Y. Uno *et al.* [94] follow the trend of evaluated data of the TENDL-2019 library. However, above 15 MeV, the reported data of Lu Hanlin *et al.* [96], H. L. Pai *et al.* [105], M. Bormann *et al.* [106] and F. Gabbard *et al.* [107] show agreement with the evaluated data within experimental uncertainties.

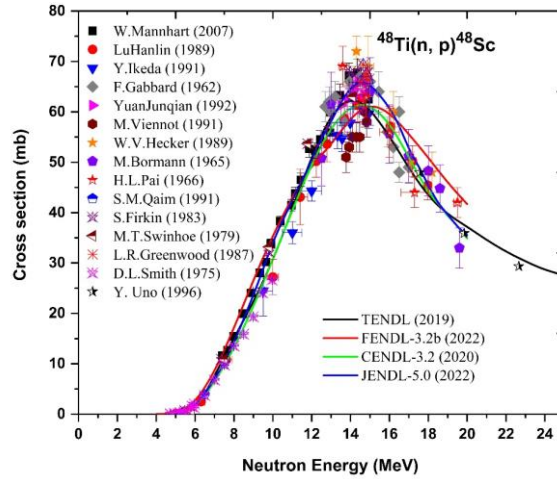


Fig. 6.17. Literature cross sections compared with the latest evaluated data libraries.

The theoretical results based on the phenomenological and microscopic level density models are presented in Figs. 6.18(a-d). Initially, for all these default calculations phenomenological and microscopic level density, preequilibrium, and optical potential models were used as mentioned in Table 6.11. The theoretical estimation of the $^{48}\text{Ti}(n, p)^{48}\text{Sc}$ reaction was compared with the previous experimental results of Ref. [94-107].

Table 6. 11 Theoretical models and optimum parameters are used in TALYS calculations to reproduce the data of ^{48}Ti isotope.

Nuclide	Level density models	Preequilibrium model	Optical potential model	Level density parameters	Keywords
^{48}Ti	Constant temperature	preeqmode 2	dispersion y	alphald 0.07996 betald 0.27276	Fullhf asys
	Back-shifted Fermi gas	preeqmode 2	jlomp y	alphald 0.07796 betald 0.18276 gammald 0.051	fullhf gshell
	Generalized superfluid	preeqmode 2	dispersion y	alphald 0.1336 betald 0.03092	Fullhf
	S. Goriely	preeqmode 3	jlomp y	ctable -0.0921 ptable 0.2741	fullhf
	S. Goriely-S. Hilaire	preeqmode 3	jlomp y	ctable -0.0921 ptable 0.2741	fullhf

	S. Goriely-S. Hilaire Gogny force	preeqmode 2	jlmomp y	ctable -0.0921 ptable 0.2741	Fullhf
--	---	-------------	----------	---------------------------------	--------

It is observed that these default theoretical results based on the phenomenological and microscopic models failed to reproduce the literature data from threshold to 25 MeV are shown in Figs. 6.18(a-b). The theoretical calculations were improved using different models and adjusting the parameters available in the TALYS code to reproduce the experimental data. The theoretical trend of the $^{48}\text{Ti}(n,p)^{48}\text{Sc}$ cross section from the statistical model calculations after adjusting the parameters is shown in Figs. 6.18(c-d). However, we have shown that the trend of the experimental data can be reproduced with a statistical model TALYS code with appropriate adjustments made to the microscopic level density parameters ‘ctable’ and ‘ptable’ [see Fig. 6.18(d)]. Similarly, the appropriate adjustments were made to the phenomenological level density parameters α_{hald} , β_{ald} and γ_{ald} to reproduce the experimental data as shown in Fig. 6.18(c). The level density parameters and the different theoretical model adjustments adapted to reproduce the previously measured experimental data are given in Table 6.11.

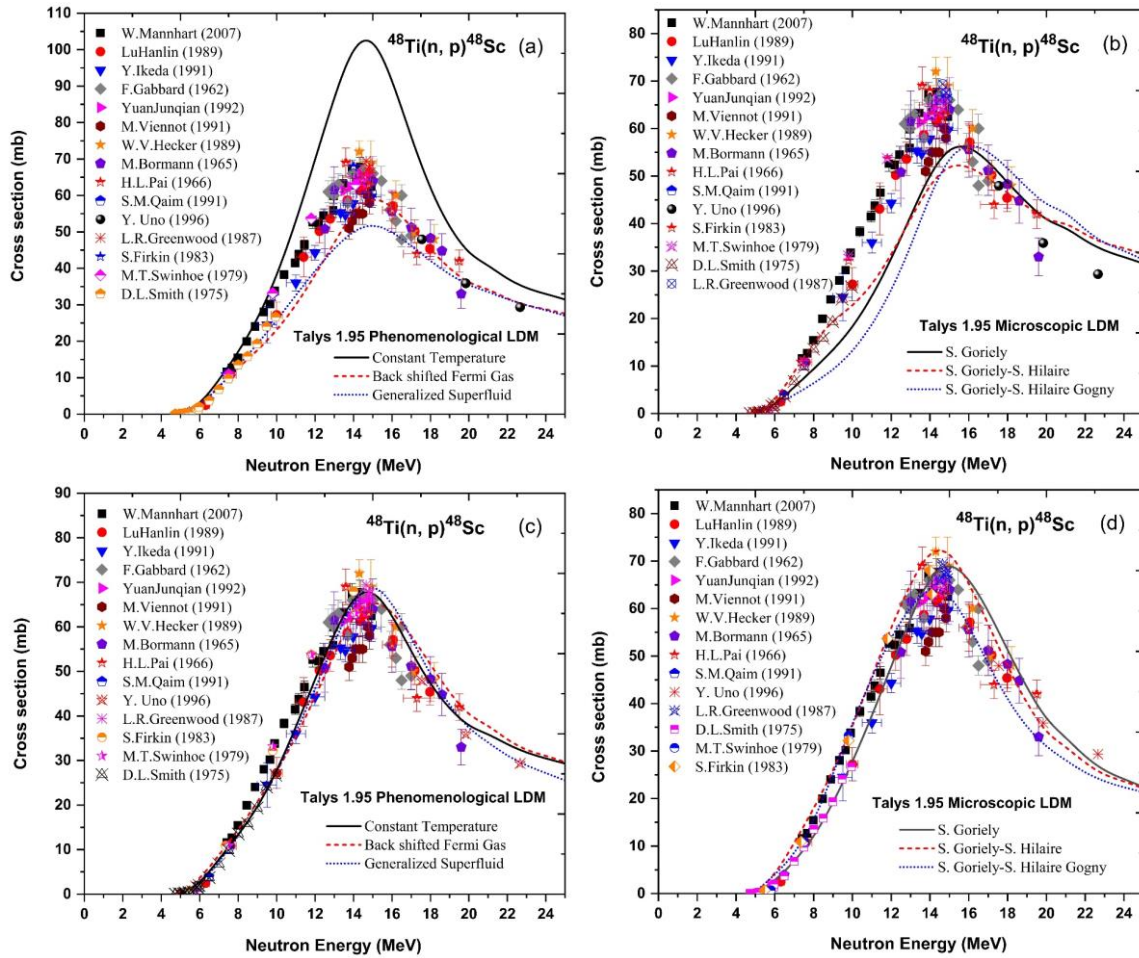


Fig. 6.18. Literature cross sections compared with the TALYS (ver. 1.95) calculations based on the phenomenological and microscopic level density models (a-b) Default and (c-d) Adjusted.

6.4. Calculation of the (n, p) reaction cross sections through systematic formulae

Vanadium, chromium, titanium and copper are the essential structural material for the fusion reactor technology, therefore charged particles (n, p) and (n, α) production reactions cross sections were calculated using different systematic formulae. The systematic formulae suggested by various authors [108-119] were used to estimate the (n, p) and (n, α) reaction cross section for the ^{48}Ti , ^{51}V , ^{52}Cr and ^{65}Cu isotopes. The cross sections obtained from systematic formulae were discussed and compared with literature data taken from the EXFOR database and with evaluations within 14 to 15 MeV neutron energies. These calculated values of cross section from formulae are given in Tables 6.12 and 6.13.

Table 6.12 The (n, p) reaction cross sections for ^{48}Ti , ^{51}V , ^{52}Cr and ^{65}Cu calculated from the systematic formulae.

Authors	$\sigma_{(n,p)} (mb)$			
	$^{48}\text{Ti}(n,p)^{48}\text{Sc}$	$^{51}\text{V}(n,p)^{51}\text{Ti}$	$^{52}\text{Cr}(n,p)^{52}\text{V}$	$^{65}\text{Cu}(n,p)^{65}\text{Ni}$
Levkovski	64.49	40.49	83.52	33.23
Ait Tahar	53.66	34.79	73.26	32.81
Luo	76.63	47.66	99.66	38.83
Habbani	35.85	25.63	49.27	21.94
Kasugai	49.12	31.46	71.37	32.54
Forrest	55.40	42.59	56.97	29.41
Doczi	75.40	58.18	79.95	54.64
Konno	59.85	40.29	75.20	34.60
Kumabe and Fukuda	61.55	39.66	82.91	36.41
E. Tel	29.14	22.34	34.59	20.90
Bychkov	28.96	18.87	39.41	17.07
EXFOR	67.75	26.94	95.90	20.40
TENDL-2019	62.05	30.54	91.53	15.53
ENDF/B-VIII.0	58.99	30.66	87.00	19.08
JENDL/AD-2017	62.00	28.19	88.51	21.50

As can be seen from Table 6.12, that $^{51}\text{V}(n, p)^{51}\text{Ti}$ reaction cross section was calculated using systematic formulae of Kasugai and Habbani agrees with EXFOR data as well as with the evaluations of TENDL-2019 and ENDF/B-VIII.0. The cross sections of the $^{48}\text{Ti}(n, p)^{48}\text{Sc}$ reaction, the formula of the Kumabe and Fukuda is agreement with the TENDL-2019 evaluation, whereas other formula failed to reproduce the experimental and evaluation data. In contrast, the formulae of the Levkovski, Ait Tahar, Luo, Forrest, Habbani, Kasugai, Forrest, Doczi, Konno, Kumabe, C. Konno, E. Tel and Bychkov predicts higher and lower values of the $^{52}\text{Cr}(n, p)^{52}\text{V}$ reaction cross sections and failed to reproduce the EXFOR and evaluated data. The (n, p) reaction cross sections of the ^{65}Cu isotope estimated by systematic formulae of Habbani, and E. Tel are in better agreement with the previous measurements of the EXFOR and JENDL/AD-2017.

The (n, α) reaction cross section from formulae of the Levkovski is in good agreement with the evaluations JENDL/AD-2017 evaluation for the $^{51}\text{V}(n, \alpha)^{48}\text{Sc}$ reaction. Similarly, the cross sections from formulae of the Habbani and Kasugai agree with the ENDF/B-VIII.0 evaluation, whereas the Konobeyev formula agrees with the TENDL-2019 evaluation. Furthermore, the calculations from the Levkovski, Ait Tahar, Luo, Kasugai, Habbani, Forrest and Konobeyev predicts lower values of the cross sections compared to the EXFOR and evaluated data for the $^{48}\text{Ti}(n, \alpha)^{48}\text{Sc}$ and $^{52}\text{Cr}(n, \alpha)^{52}\text{V}$ reactions. In addition, the cross sections of the $^{65}\text{Cu}(n, \alpha)^{65}\text{Ni}$ reaction, the formula of Habbani and Kasugai reproduce the ENDF/B-V.III.0 evaluation.

Table 6.13 The (n, α) reaction cross sections for ^{48}Ti , ^{51}V , ^{52}Cr and ^{65}Cu calculated from the systematic formulae.

Authors	$\sigma_{(n, \alpha)} (mb)$			
	$^{48}\text{Ti}(n, \alpha)^{48}\text{Sc}$	$^{51}\text{V}(n, \alpha)^{48}\text{Sc}$	$^{52}\text{Cr}(n, \alpha)^{52}\text{V}$	$^{65}\text{Cu}(n, \alpha)^{65}\text{Ni}$
Levkovski	26.27	17.12	33.47	14.41
Ait Tahar	22.43	14.89	30.41	14.17
Luo	24.94	15.46	32.48	12.57
Habbani	45.93	29.94	49.85	19.48
Kasugai	35.59	24.77	41.69	19.52
Forrest	34.20	25.43	36.14	17.35
Konobeyev	33.62	20.24	42.66	15.12
EXFOR	67.75	16.91	77.51	20.40
TENDL-2019	62.05	16.26	91.53	15.53
ENDF/B-VIII.0	58.99	16.25	87.00	19.07
JENDL/AD-2017	62.00	17.21	88.52	21.51

The (n, p) reaction cross section for selenium isotopes using systematic formula is given in Table 6.14, the calculated cross section based on the Kasugai, Luo, Ait Tahar, Levkovski and Doczi formulae shows good agreement with the EXFOR data [48-50,55], whereas Forrest and Habbani formulae produced cross section very low compared to the EXFOR data. The cross section of $^{77}\text{Se}(n, p)^{77}\text{As}$ reaction from the EXFOR data [49] shows good agreement with Doczi formula, whereas the cross section calculated by other formulae are very low compared to the EXFOR data. It is observed that the cross section for the $^{78}\text{Se}(n, p)^{78}\text{As}$ reaction from Kasugai, Luo, Ait Tahar, Levkovski and Forrest authors shows a good agreement with the EXFROR data [48-56], whereas Habbani formula produced very

low cross section compared to the EXFOR data. Similarly, the cross section for the $^{80}\text{Se}(n,p)^{80}\text{As}$ reaction from the EXFOR data [50, 9] shows good agreement with the Levkovski, Ait Tahar, Luo and Kasugai calculations, whereas Doczi and Forrest calculated value is very high compared to the EXFOR data. On the other hand, the value from the Habbani formula is very low compared to the EXFOR data.

This comparison and discussion improve activation cross sections for essential structural Vanadium, Copper, Titanium and Chromium materials and helpful in the validation of different systematic formulae within 14-15 MeV energies.

Table 6.14 The (n,p) reaction cross sections for ^{76}Se , ^{77}Se , ^{78}Se and ^{80}Se calculated from the systematic formulae.

Authors	$\sigma_{(n,p)}$ (mb)			
	$^{76}\text{Se}(n,p)^{76}\text{As}$	$^{77}\text{Se}(n,p)^{77}\text{As}$	$^{78}\text{Se}(n,p)^{78}\text{As}$	$^{80}\text{Se}(n,p)^{80}\text{As}$
Levkovski	39.23	26.67	18.32	8.89
Ait Tahar	41.89	28.43	19.49	9.42
Luo	45.95	31.01	21.14	10.12
Habbani	28.01	19.02	13.04	6.31
Kasugai	45.48	29.63	19.37	8.41
Doczi	50.73	38.67	29.54	17.34
Forrest	24.24	22.32	21.68	23.58
Konno	40.39	29.01	40.39	11.31
Kumabe and Fukuda	46.23	31.55	46.23	10.63
E. Tel	23.88	19.01	23.88	9.94
Bychkov	23.48	14.67	23.48	3.71
EXFOR	50.5	65.4	19.1	11.1
TENDL-2019	54.71	49.32	25.39	12.83
ENDF/B-VIII.0	69.99	36.51	18.02	14.74
JENDL-5.0	57.05	37.48	19.78	15.26

6.5. Summary and Conclusions

In conclusion, the cross sections of the $^{76}\text{Se}(n,p)^{76}\text{As}$, $^{77}\text{Se}(n,p)^{77}\text{As}$, $^{78}\text{Se}(n,p)^{78}\text{As}$, $^{80}\text{Se}(n,p)^{80}\text{As}$, $^{51}\text{V}(n,p)^{51}\text{Ti}$ and $^{65}\text{Cu}(n,p)^{65}\text{Ni}$ reactions were measured at different incident neutron energies using quasi-monoenergetic neutron produced via the $^7\text{Li}(p,n)$ reaction. The cross section was measured relative to the $^{27}\text{Al}(n,\alpha)^{24}\text{Na}$ reference reaction using the neutron activation method and off-line γ -ray spectrometry technique using latest decay data. The correction factors are taken into consideration due to γ -ray self-attenuation, geometry correction and low energies background neutrons. In the present work, a method of covariance analysis was executed to estimate the uncertainties in measured cross sections using micro-correlation and error analysis method. The uncertainties in the HPGe detector efficiency and measured cross section were calculated using the covariance analysis method. The uncertainties in the measured (n,p) reaction cross sections are in the range of 6–24%.

The present measurements of cross section were compared with the literature data taken from the EXFOR compilation and evaluations of the FENDL-3.2, FENDL-3.2b, CENDL-3.2, JEFF-3.3, JENDL-4.0/HE, JENDL-4.0, JENDL-5.0, JENDL/AD-2017, ENDF/B-VIII.0 and TENDL-2019 libraries. Some of the present data have been measured for the first time, whereas the rest of the data show agreement with the literature data, evaluated data of different libraries, as well as the theoretical values obtained from statistical reaction codes. Moreover, the (n,p) and (n,α) reactions cross sections for the structure material Vanadium, Copper, Titanium and Chromium were also calculated using the different systematic formulae predicted by several authors to investigate available data and validate the formulae within the 14-15 MeV neutron energies region. The cross section calculated from the systematic formulae of Kasugai, Luo, Ait Tahar, Levkovski, Habbani, Konobeyev and Forrest show good agreement with the literature data.

Theoretical calculations were performed using the TALYS and EMPIRE codes from the reaction threshold to 25 MeV neutron energies. The present and previous measurements were used to validate the theoretical values based on the TALYS and EMPIRE codes by considering the level density, optical potential, and preequilibrium models. The impacts of various combinations of the nuclear input parameters of different level density models, optical model potentials, and preequilibrium models were also considered. The computed cross sections were found to be similar to the observed data when specific level density

models were applied. Moreover, the impacts of optical model potential and γ -ray strength functions were much less than those of nuclear level densities.

The present measurements of the (n,p) reaction provide important support for verifying the accuracy of nuclear models used in the calculation of cross sections and for the design and construction of fusion/fission reactors, and other related nuclear engineering calculations. The present work will be helpful to improve the activation cross sections for fusion reactor material Vanadium, Copper, Titanium and Chromium, advance reactor design and verification of nuclear reaction models in higher neutron energy regions. The present research activity should be extended in the neutron energies region given that the existing experimental information is limited. In this way, a more systematic investigation of the theoretical calculations can be achieved. This work has contributed to the understanding of (n,p) reaction on the $^{76,77,78,80}\text{Se}$, ^{65}Cu , ^{52}Cr , ^{51}V and ^{48}Ti isotopes.

Bibliography

- [1] J. B. Hicks, Toroidal field system for tight aspect ratio tokamak reactors, Culham Laboratory Report, AEA FUS Report No. 118, 1991 (unpublished).
- [2] Accelerator-driven Systems and Fast Reactors in Advanced Nuclear Fuel Cycles, OECD Nuclear Energy Agency 2002,
<http://www.nea.fr/html/ndd/reports/2002/nea3109.html>
- [3] B. Lalemruata, N. Otuka, G.J. Tambave *et al.*, Phys. Rev. C 85, 024624 (2012).
- [4] O. K. Harling, G. P. Yu, N. J. Grant, and J. E. Meyer, J. Nucl. Mater. 104, 127 (1981).
- [5] U.S. Department of Energy, Proceedings of the Workshop on Copper and Copper Alloys for Fusion Reactor Applications, 1983 (unpublished).
- [6] D. L. Smith, B. A. Loomis, *et al.*, Journal of Nuclear Materials 135, 125-139 (1985).
- [7] Jia Huang, Haocheng Liu, *et al.*, Frontiers in Materials, Volume 9 – 849115, 2022.
- [8] R. J. Livak, T. G. Zocco *et al.*, Journal of Nuclear Materials 144 121-127 (1987).
- [9] F.M.D. Attar, S.D. Dhole, V.N. Bhoraskar *et al.*, Phys. Rev. C 90, 064609 (2014)
- [10] N. Otukaa, E. Dupont, V. Semkov *et al.*, Nucl. Data Sheets 120, 272 (2014).
- [11] D. A. Brown, M. B. Chadwick, R. Capote *et al.*, Nucl. Data Sheets 148, 1 (2018).
- [12] P. Pereslavtsev, A. Konobeyev *et al.*, JEFF-3.3, Evaluation nuclear data library of the OECD Nuclear Energy Agency, JEF/DOC, 2017, p. 1864.

- [13] S. Kunieda *et al.*, Overview of JENDL-4.0/HE and benchmark calculation, JAEA Conf. Proc. No. 2016-004 (2016), pp. 41–46.
- [14] K. Shibata, O. Iwamoto, T. Nakagawa, N. Iwamoto, A. Ichihara, *et al.*, “JENDL-4.0, A New Library for Nuclear Science and Engineering,” J. Nucl. Sci. Technol. 48, 1 (2011).
- [15] K. Shibata, N. Iwamoto, S. Kunieda, *et al.*, “JENDL/AD-2017” “Activation Cross-section File for Decommissioning of LWRs” JAEA-Conf 2016-004, pp.47-52.
- [16] O. Iwamoto, *et al.*, "Japanese Evaluated Nuclear Data Library version 5: JENDL-5.0", to be submitted (2022).
- [17] K. Xu, H. X. An, *et al.*, CENDL-3.2 Chinese evaluation neutron data library, (2020).
- [18] A. J. Koning, D. Rochman, *et al.*, TENDL-2019, Nucl. Data Sheets 155, 1 (2019).
- [19] R. A. Forrest, R. Capote, N. Otsuka *et al.*, FENDL-3.2 Fusion Evaluation Nuclear Data Library, IAEA INDC Report No. NDS-0628, 2021 (unpublished).
- [20] R. A. Forrest, R. Capote, N. Otsuka, *et al.*, FENDL-3.2b Fusion Evaluation Nuclear Data Library, IAEA, INDC (NDS)-0628 (2022).
- [21] A. J. Koning *et al.*, TALYS (ver. 1.9), A nuclear reaction program, user manual, NRG-1755 ZG Petten, The Netherlands (2018).
- [22] M. Herman, R. Capote, M. Sin *et al.*, Nucl. Data Sheets 108, 2655 (2007).
- [23] W. Hauser and H. Feshbach, Phys. Rev. 87, 366 (1952).
- [24] C. Kalbach, Phys. Rev. C 33, 818 (1986).
- [25] A. J. Koning and M. C. Duijvestijn, Nucl. Phys. A. 744, 15 (2004).
- [26] A. J. Koning and J. P. Delaroche, Nucl. Phys. A. 713, 231 (2003).
- [27] E. Bauge, J. P. Delaroche, and M. Girod, Phys. Rev. C 63, 024607 (2001).
- [28] R. Capote, M. Herman *et al.*, RIPL-3, Nuclear Data Sheets 110, 3107 (2009).
- [29] D. M. Brink, Nucl. Phys. 4, 215 (1957).
- [30] P. Axel, Phys. Rev. 126, 671 (1962).
- [31] J. Kopecky and M. Uhl, Phys. Rev. C 41, 1941 (1990).
- [32] A. Gilbert and A. G. W. Cameron, Can. J. Phys. 43, 1446 (1965).
- [33] W. Dilg, W. Schantl, H. Vonach, and M. Uhl, Nucl. Phys. A 217, 269 (1973).
- [34] A. V. Ignatyuk, K. K. Istekov *et al.*, Sov. J. Nucl. Phys. 29, 450 (1979).
- [35] A. V. Ignatyuk, J. L. Weil, S. Raman, and S. Kahane, Phys. Rev. C 47, 1504 (1993).
- [36] S. Hilaire, M. Girod, S. Goriely, and A. J. Koning, Phys. Rev. C 86, 064317 (2012).

- [37] S. Goriely, F. Tondeur, and J. M. Pearson, *Atom. Nucl. Data Tables* 77, 311 (2001).
- [38] S. Goriely, S. Hilaire, and A. J. Koning, *Phys. Rev. C* 78, 064307 (2008).
- [39] J. Raynal, *Computing as a language of physics*, ICTP International Seminar Course, IAEA, ICTP, Trieste, Italy (1972).
- [40] H. M. Hofmann, J. Richert, J. W. Tepel *et al.*, *Ann. Phys. (NY)* 90, 403 (1975).
- [41] J. W. Tepel, H. M. Hofmann, and H. A. Weidenmuller, *Phys. Lett. B* 49, 1 (1974).
- [42] H. M. Hofmann, T. Mertelmeier, *et al.*, *Z. Phys. A* 297, 153 (1980).
- [43] V. A. Plujko, *Acta Phys. Pol. B* 31, 435 (2000).
- [44] H. Nishioka, J. J. M. Verbaarschot, and S. Yoshida, *Ann. Phys. (NY)* 172, 67 (1986).
- [45] T. Tamura, T. Udagawa, and H. Lenske, *Phys. Rev. C* 26, 379 (1982).
- [46] J. J. Griffin, *Phys. Rev. Lett.* 17, 478 (1966).
- [47] M. Blann, *Phys. Rev. C* 54, 1341 (1996).
- [48] Birn, I., & Qaim, S. M. Excitation Functions of Neutron Threshold Reactions on Some Isotopes of Germanium, Arsenic, and Selenium in the 6.3 to 14.7-MeV Energy Range. 5639 (October) (2017).
- [49] H. M. Hoang, U. Garuska, *et al.*, *Z. Phys. Atomic Nuclei* 334, 285-291 (1989).
- [50] A. A. Filatenkov *et al.*, *Khlopin Radiiev. Inst. Report No. 258*, (1999).
- [51] Guozhu He, *et al.*, *Indian Journal of Pure and Applied Physics*, Vol. 43, p.729 (2005).
- [52] B. Minetti and A. Pasquarelli, *Nuclear Physics A.100* (1967).
- [53] P. Venugopala Rao And R. W. Fink, *Physical Review*, Vol. 154, No. 4 (1967).
- [54] N. I. Molla and S. M. Qaim, *Nuclear Physics A283*, 269-288 (1977).
- [55] A. Grallert, *et al.*, *IAEA Nucl. Data Section report to the I.N.D.C. No.286*, p.131 (1993).
- [56] V. V. Ivanenko and K. A. Petrzhak, *Yadernaya Fizika Vol.9, Issue.2*, p.258 (1969).
- [57] A. Gandhi, A. Sharma, A. Kumar, *et al.*, *Phys. Rev. C* 102, 014603 (2020).
- [58] A. A. Filatenkov, R, *INDC (CCP)-0460* (2016).
- [59] M. Furutaa, T. Shimizua *et al.*, *Ann. Nucl. Energy* 35, 1652 (2008).
- [60] W. Mannhart and D. Schmidt, R, *PTB-N-53* (2007).
- [61] A. K. M. Harun-Ar-Rashid *et al.*, *Indian J. Phys.* 80, 737 (2006).
- [62] Toshiaki Shimizua, Hitoshi Sakane *et al.*, *Ann. Nucl. Energy* 31, 975 (2004).

- [63] N. I. Molla and S. M. Qaim, Nucl. Phys. A 283, 269 (1977).
- [64] Y. Ikeda, C. Konno, K. Oishi et al., JAERI Report No. 1312, 1988 (unpublished).
- [65] P. N. Ngoc, S. Gueth, *et al.*, Ph.D. thesis, Eotvos Lorand Univ., Budapest Hungary, 1980.
- [66] T. B. Ryves, P. Kolkowski, and K. J. Zieba, Metrologia 14, 127 (1978).
- [67] G. N. Maslov, F. Nasyrov, et al., USSR report to the INDC, 1974 (unpublished), p. 10.
- [68] I. G. Clator, Ph.D. thesis, University of West Virginia, USA, 1969.
- [69] D. C. Santry and J. P. Butler, Can. J. Phys. 44, 1183 (1966).
- [70] M. Bormann, S. Cierjacks et al., Z. Phys. 174, 1 (1963).
- [71] Yoshitomo Uwamino, Nucl. Sci. Eng. 111, 391 (1992).
- [72] S. M. Grimes, R. C. Haight, K. R. Alvar, *et al.*, Phys. Rev. C 19, 2127 (1979).
- [73] I. Pasha, B. Rudraswamy, *et al.*, Radiochimica Acta, Vol. 108, p. 679 (2020).
- [74] W. Mannhart, *et al.*, Phys. Techn. Bundesanst., Neutronenphysik Reports, No. 53 (2007).
- [75] A. Fessler, E. Wattecamps, *et al.*, Phys. Rev. Part C, Vol. 58, p.996 (1998).
- [76] Y. Kasugai, *et al.*, Annals of Nuclear Energy, Vol. 25, Issue.1-3, p.23 (1998).
- [77] Y. Ikeda, C. Konno, K. Oishi, T. Nakamura, et al., JAERI Reports, No.1312 (1988)
- [78] S. K. Ghorai, J. R. Williams, and W. L. Aford, J. Phys. G 13, 405 ~1987.
- [79] M. Viennot, A. Ait Haddou, G. Paic Conf. on Nucl. Data for Sci. and Technol., Antwerp 1982, p.406 (1982).
- [80] D. L. Smith and J. W. Meadows, Nucl. Sci. Eng. 76, 43~(1980).
- [81] I. G. Clator, "Neutron induced reactions between 14.4 and 16.7 MeV", Thesis, (1969).
- [82] B. D. Kern, W. E. Thompson, and J. Ferguson, Nucl. Phys. 10, 226 ~(1959).
- [83] Y. Ikeda, C. Konno, K. Oishi, T. Nakamura, *et al.*, Report No. JAERI-1312 (1988)
- [84] A. Fessler, *et al.*, Nuclear Science and Engineering 134, 171–200 (2000).
- [85] D. L. Smith, *et al.*, Ann. nucl. Energy, Vol. 11, No. 12, pp. 623 627, (1984).
- [86] M. Bormann, S. Cierjacks *et al.*, Zeitschrift fiir Physik 174, 1-17 (1963).
- [87] Masataka Furuta, *et al.*, Annals of Nuclear Energy, Vol. 35 1652–1662 (2008).
- [88] Toshiaki Shimizu, *et al.*, Annals of Nuclear Energy 31 975–990 (2004).
- [89] T. Katoh, K. Kawade, H. Yamamoto, Report No. JAERI-M-89-083 (1989).

- [90] Yoshitomo Uwamino, Hiroshi Sugita, *et al.*, Nucl. Sci. and Engi. 111 , 391-403 (1992).
- [91] Kaihong Fanga, Shiwei Xua, Changlin Lan, Applied Radiation and Isotopes 66 1104–1107 (2008).
- [92] W. Mannhart, *et al.*, Phys. Techn. Bundesanst., Neutronenphysik Reports, No. 53 (2007).
- [93] P. Reimer, V. Avrigeanu, A. J. M. Plompen *et al.* Phys. Rev. C, 65, 014604 (2001).
- [94] Y. Uno, *et al.*, Internat. Symposium on Reactor Dosimetry, Prague, 1996, p.465 (1996).
- [95] Yuan Junqian, *et al.*, High Energy Physics and Nucl. Physics, Chinese ed., Vol. 16, Issue.1, p.57 (1992).
- [96] Lu Hanlin, Zhao Wenrong, et al. Chinese report to the I.N.D.C., No.16 (1989).
- [97] Y. Ikeda, *et al.*, Conf. on Nucl. Data for Sci. and Technol., Juelich 1991, p.294 (1991).
- [98] S. M. Qaim, *et al.*, Conf. on Nucl. Data for Sci. and Technol., Juelich 1991, p.297 (1991).
- [99] M. Viennot, *et al.*, S. Joly, Nuclear Science and Engineering, Vol. 108, p.289 (1991).
- [100] W. V. Hecker, *et al.*, Nucl. Instru. Meth. in Phys. Res., Sect. B, Vol.40-41, p.478 (1989).
- [101] L. R. Greenwood, American Soc. of Testing and Materials Report, No. 956, p.743 (1987).
- [102] S. Firkin A.E.R.E. Harwell Reports, No.3350 (1983).
- [103] M. T. Swinhoe, C. A. Uttley, A.E.R.E. Harwell Reports, No. 26, p.39 (1979).
- [104] D. L. Smith, J. W. Meadows, Nuclear Science and Engineering, Vol. 58, p.314 (1975).
- [105] H. L. Pai, Canadian Journal of Physics, Vol. 44, p.2337 (1966).
- [106] M. Bormann, E. Fretwurst, P. Schehka, *et al.*, Nuclear Physics, Vol. 63, p.438 (1965).
- [107] F. Gabbard, B. D. Kern, Physical Review, Vol. 128, p.1276 (1962).
- [108] J. Luo *et al.*, Nucl. Instrum. Methods B, 266, 4862 (2008).
- [109] R. A. Forrest and J. Kopecky, Fusion Eng. Des. 82, 73 (2007).
- [110] E. Tel, B. Sarer, S. Okuducu *et al.*, J. Phys. G: Nucl. Part. Phys. 29, 2169 (2003).
- [111] F. I. Habbani and Khalda T. Osman, Appl. Radiat. Isot. 54, 283 (2001).
- [112] R. Doczi, *et al.*, IAEA-NDS Report No. Indc (HUN)-032, 1997 (unpublished).
- [113] Y. Kasugai, Y. Ikeda, H. Yamamoto, and K. Kawade, in Proceedings of the 1994 Symposium on Nuclear Data, 1995 (unpublished).

- [114] C. Konno, Y. Ikeda, K. Osihi, *et al.*, JAERI Report No. 1329, 1993 (unpublished).
- [115] I. Kumabe and K. J. Fukuda, Nucl. Sci. Tech. 24, 83 (1987).
- [116] S. Ait-Tahar, J. Phys. G: Nucl. Phys. 13, L121 (1987).
- [117] V. M. Bychkov, *et al.*, IAEA-NDS Report No. Indc (CCP), 1980 (unpublished), p. 146.
- [118] V. N. Levkovski, Zh. Eksp. Teor. Fiz. 45, 305 (1963) [JETP 18, 213 (1964)].
- [119] A. Yu. Konobeyev, V. P. Lunev, *et al.*, Nucl. Instrum. Methods B 108, 233 (1996).